Int J Appl Earth Obs Geoinformation 93 (2020) 102217

Contents lists available at ScienceDirect

Int J Appl Earth Obs Geoinformation

journal homepage: www.elsevier.com/locate/jag

Monitoring active open-pit mine stability in the Rhenish coalfields of Germany using a coherence-based SBAS method

Wei Tang[a,b,*], Mahdi Motagh[b,c], Wei Zhan[d]

[a] College of Geoscience and Surveying Engineering, China University of Mining and Technology, Beijing 100083, China
[b] Helmholtz Centre Potsdam, GFZ German Research Centre for Geosciences, Department of Geodesy, Section of Remote Sensing and Geoinformatics, Potsdam 14473, Germany
[c] Institute of Photogrammetry and Geoinformation, Leibniz University Hannover, Hannover 30167, Germany
[d] The First Monitoring and Application Center, China Earthquake Administration, Tianjin 300180, China

ARTICLE INFO

Keywords:
InSAR
open-pit mine
slope instability
ground deformation

ABSTRACT

With the recent progress in synthetic aperture radar (SAR) technology, especially the new generation of SAR satellites (Sentinel-1 and TerraSAR-X), our ability to assess slope stability in open-pit mines has significantly improved. The main objective of this work is to map ground displacement and slope instability over three open-pit mines, namely, Hambach, Garzweiler and Inden, in the Rhenish coalfields of Germany to provide long-term monitoring solutions for open-pit mining operations and their surroundings. Three SAR datasets, including Sentinel-1A data in ascending and descending orbits and TerraSAR-X data in a descending orbit, were processed by a modified small baseline subset (SBAS) algorithm, called coherence-based SBAS, to retrieve ground displacement related to the three open-pit mines and their surroundings. Despite the continuously changing topography over these active open-pit mines, the small perpendicular baselines of both Sentinel-1A and TerraSAR-X data were not affected by DEM errors and hence could yield accurate estimates of surface displacement. Significant land subsidence was observed over reclaimed areas, with rates exceeding 500 mm/yr, 380 mm/yr, and 310 mm/yr for the Hambach, Garzweiler and Inden mine, respectively. The compaction process of waste materials is the main contributor to land subsidence. Land uplift was found over the areas near the active working parts of the mines, which was probably due to excavation activities. Horizontal displacement retrieved from the combination of ascending and descending data was analysed, revealing an eastward movement with a maximum rate of ~120 mm/yr on the western flank and a westward movement with a maximum rate of ~60 mm/yr on the eastern flank of the pit. Former open-pit mines Fortuna-Garsdorf and Berghein in the eastern part of Rhenish coalfields, already reclaimed for agriculture, also show subsidence, at locations reaching 150 mm/yr. The interferometric results were compared, whenever possible, with groundwater information to analyse the possible reasons for ground deformation over the mines and their surroundings.

1. Introduction

Ground surface deformation, such as slope instability and land subsidence, is one of the most critical issues in the mining industry. Land subsidence occurring in underground mining areas may adversely affect the safety of built structures and impede economic development. Extremely high and steep slopes are very common in open-pit mines, which are prone to slope failures (Hu, 2013) that can endanger the lives of workers and cause enormous economic losses. On July 18, 2009, a massive landslide on the southern shore of Lake Concordia in central Germany carried three houses away, killing three people (Vinzelberg and Dahmen, 2014). An investigation found that high pressure in the aquifer, combined with loose dump material underwater, was to blame for the accident. On April 10, 2013, a massive landslide occurred at the Bingham Canyon Mine in the western state of Utah in the United States. Approximately 65×10^6–70×10^6 m^3 of dirt and rock moved down the side of the pit. An interferometric radar system was previously installed to monitor the ground's stability and produced warnings before the landslide (NASA, 2020). Therefore, mining operations were stopped before the slide occurred; as a result, there were no injuries. Another recent case occurred in Myanmar, where at least 27 people died following a landslide at a jade mine in a remote area of Kachin state (SCMP, 2018). This mine is poorly regulated, lacks an effective system to monitor slope instability and is frequently hit by fatal disasters. The

* Corresponding author.
E-mail address: weitang@cumtb.edu.cn (W. Tang).

https://doi.org/10.1016/j.jag.2020.102217
Received 21 February 2020; Received in revised form 24 July 2020; Accepted 5 August 2020
Available online 18 August 2020

lessons we can learn from slope failure accidents are that many lives can be saved if the right monitoring system is installed and the time of failure can be forecasted (Carlà et al., 2018). Another important lesson is that small surface movements on a mine high wall may be a sign of instability that presages slope failure. Therefore, the effective monitoring and management of mining-induced ground deformations is very important for the mining industry.

Currently, conventional surveying techniques using levelling techniques, theodolites, total stations, and GPS, or geotechnical methods, such as extensometers, inclinometers, piezometers and crack measuring pins, are the main deformation monitoring systems used over mining areas (Hu, 2013; Paradella et al., 2015). The advantages of the abovementioned techniques are their direct observations and high accuracy. However, they are difficult to mount on dangerous areas and cannot cover the whole target of interest. Furthermore, a mine bench is not permanent, as dynamic excavation processes limit the use of contact measurement techniques in open-pit mines.

Space geodetic techniques are particularly useful for determining the extent and current state of ground displacement over mining areas, with many benefits arising from the use of synthetic aperture radar (SAR) data (Zhu et al., 2020). Differential interferometric SAR (DInSAR) permits the remote detection of surface deformation at high precision over large areas without field access requirements (Burgmann et al., 2000; Massonnet et al., 1993; Massonnet and Feigl, 1998; Peltzer and Rosen, 1995).

A single interferogram generated using only two SAR images has limitations due to temporal and geometrical decorrelations and atmospheric artefacts. Advanced DInSAR methods, which are based on the processing of multitemporal SAR images, were developed to overcome these drawbacks. They include persistent scatterer InSAR (PSInSAR) (Crosetto et al., 2016; Ferretti et al., 2001; Hooper et al., 2007) and small baseline subset (SBAS) methods (Berardino et al., 2002; Osmanoğlu et al., 2016). These advanced techniques allow for detecting millimetre-scale displacements over long periods by carefully reducing other noises such as atmospheric disturbances, orbital errors, and DEM errors. DInSAR and advanced InSAR time-series techniques have been widely used in monitoring the ground deformation associated with earthquakes (Funning et al., 2007; Massonnet et al., 1993; Ross et al., 2019; Motagh et al., 2015), volcanic eruptions (Schaefer et al., 2019; Walter et al., 2019), and landslides (Dong et al., 2018; Liu et al., 2012; Motagh et al., 2013; Wasowski and Bovenga, 2014). They are also used to monitor groundwater-induced subsidence (Haghshenas Haghighi and Motagh, 2019; Motagh et al., 2017, 2008, 2007; Tang et al., 2016), glacier movements (Sánchez-Gámez and Navarro, 2017), and nuclear tests (Wang et al., 2018). These advanced InSAR techniques have also been used for ground deformation monitoring in underground and open-pit mining areas (Carlà et al., 2017; Colombo and Macdonald, 2015; Mura et al., 2016; Przylucka et al., 2015;Yang et al., 2017a, 2017b;Zhang et al., 2015a, 2015b). However, the resolutions (10-30 m) and long revisit times (24-, 35-, and 46-day repeats) prevent this technique from becoming commonly applied in the mining industry (Esch et al., 2020, 2019), and only recently have a few studies evaluated the potential of data from the Sentinel-1A/B satellite constellation for early warning and aiding decision making in an open-pit mine (Intrieri et al., 2019).

SAR images have become more available and more frequent as the acquisition rate decreased to six days with the launch of the Sentinel-1A/B satellites. In addition, commercial SAR data services, including TerraSAR-X, COSMO-Skymed and Radarsat-2, provide image acquisitions at high spatial resolution (routinely 3 m and can achieve 1 m in spotlight mode). The shorter revisit time (up to daily in the case of COSMO-Skymed acquisition in tandem mode) and the higher spatial resolution of current SAR missions provide an improved deformation definition for mining facilities. In mining areas, InSAR technique applications are attractive because they provide non-contact, high-resolution, high-accuracy, and wide-coverage measurements. Combined with in situ measurements, InSAR can provide complementary information to document the temporal evolution of the deformation over mining areas and thus reduce the risk of significant damage to the surrounding infrastructure and environment (Colombo and Macdonald, 2015).

The main objective of this work is to evaluate the capability of Sentinel-1 and TerraSAR-X data to investigate the slope instabilities and land subsidence over three open-pit mines (Hambach, Garzweiler, and Inden) in the Rhenish coalfields of Germany. A modified SBAS algorithm (called coherence-based SBAS) was used to process three stacks of SAR images, including Sentinel-1 and TerraSAR-X, from both ascending and descending orbits to generate accurate surface displacement maps over the mines. The deformation accuracy is limited when using SAR images from conventional satellites (such as ERS and Envisat) because significant DEM errors could remain in the differential interferograms due to the large perpendicular baselines. In this study, we also show that the small perpendicular baselines of Sentinel-1 data would cause very small DEM error in the deformation results, even at the active open-pit mines where surface topography is continuously changing due to mining activities. The performance of InSAR for slope instability analysis was then evaluated by analysing the horizontal components of displacement retrieved from a combination of ascending and descending datasets. Finally, the results were compared with groundwater information to analyse the possible reasons for ground deformation over the mines and their surroundings.

2. Study sites and SAR datasets

2.1. General information

The Rhenish coalfield is located in Germany's most densely populated state of North Rhine-Westphalia between Aachen and Cologne. Three large open-pit mines are operated in this district—Hambach, Garzweiler, and Inden (Fig. 1)—by RWE Power AG to extract lignite (also known as brown coal). Coal mining and related industries have shaped the landscape in North Rhine-Westphalia for over 100 years. Some villages had to be relocated to make room for the expanding lignite mines. The current operating area of the mine is 9,000 ha (as of end of 2017), offering a total capacity of 120 Mt/y of lignite if required (RWE, 2018).

The Hambach mine is the largest open pit in Germany, with an operating area of 4,380 ha that produces approximately 40 Mt/y of brown coal. It is also the deepest mine in Germany; the bottom of the pit is 293 metres below sea level, which is equivalent to 399 metres below the ground surface (Hu, 2013) and forms an artificial depression in North Rhine-Westphalia. It is estimated that 1772 million tons of brown coal are still available, and mining operations are scheduled to continue until the middle of this century. The Garzweiler mine, located north of the Hambach mine, is part of the large brown-coal district in the Rhenish coalfield. The core of the operation—known as Garzweiler I (eastern sector)—began production in 1940, and Garzweiler II (western sector) began production in 2006 (see Fig. 1). The Garzweiler II sector occupies approximately 3,200 ha and produces approximately 30 Mt/y of lignite. It replaced the capacity from Bergheim and Garzweiler I, which were already worked out. The Inden open-pit mine is located in the southwest of the Hambach mine. With an output of approximately 20 Mt/y of brown coal, the Inden mine provides the lignite supply for the neighbouring Weisweiler power plant. The service lives of these open-pit mines will continue until 2030 for Inden and until 2045 for Garzweiler and Hambach.

2.2. Deforestation over the Hambach mine

The first mine excavation began in 1978. This was accompanied by the resettlement of local villages and towns. The Hambach Forest, the largest forest area in the region, was largely cut down to make space for

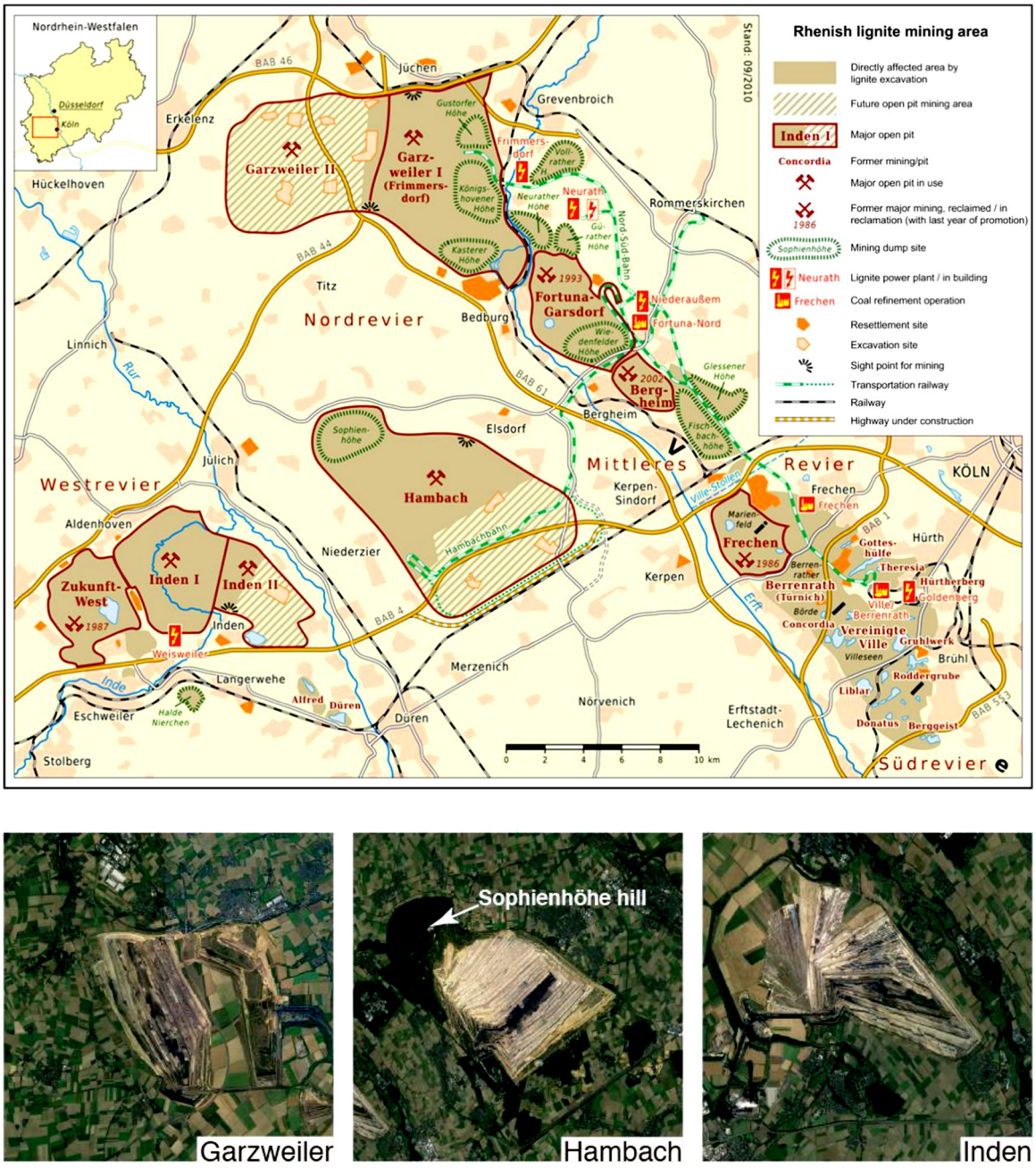

Fig. 1. Overview of the Rheinish lignite mining area with the Hambach, Garzweiler and Inden open-pit mines; Thomas Roemer (OpenStreetMap data), modified from (Hu, 2013). The three lower optical images are from Google Earth.

expanding mining projects. Before the start of mining, the Hambach Forest covered an area of 5,500 hectares. It is reported that only 1,100 hectares are left today, and the remaining forest is severely threatened by mining exploration (Donahue, 2018). As seen from the optical images in Fig. 2, the landscape of the Hambach mine has significantly changed over the last three decades due to mining activities. Since 2012, there have been ongoing protests and occupations by environmentalists to prevent mining and deforestation activities. They seek to close the mine and save the remaining sections of the forest, which are under threat of being cut down to allow for the expansion of the mine.

2.3. Available SAR images

To investigate the ground deformation, we collected three stacks of SAR images: 29 Sentinel-1A (S1A) images in ascending geometry, 42 S1A images in descending geometry, and 27 TerraSAR-X (TSX) images in descending geometry. The parameters of the SAR datasets are shown in Table 1. S1A and TSX satellites operate on different frequency bands; thus, they have different sensitivities to ground displacement, atmosphere and vegetation. TSX is sensitive to slow and small displacements due to its shorter wavelength and higher spatial resolution, but it is more prone to temporal decorrelation. The short repeat period of both sensors (12 days for S1A, 11 days for TSX) increases their ability to monitor deformation with high gradients in mining areas. However, the short wavelengths of both S1A and TSX imply a likely loss of coherence, especially when the study area is covered with dense vegetation. SAR datasets with different viewing geometries are necessary to document the different components of the ground displacements in open-pit mines.

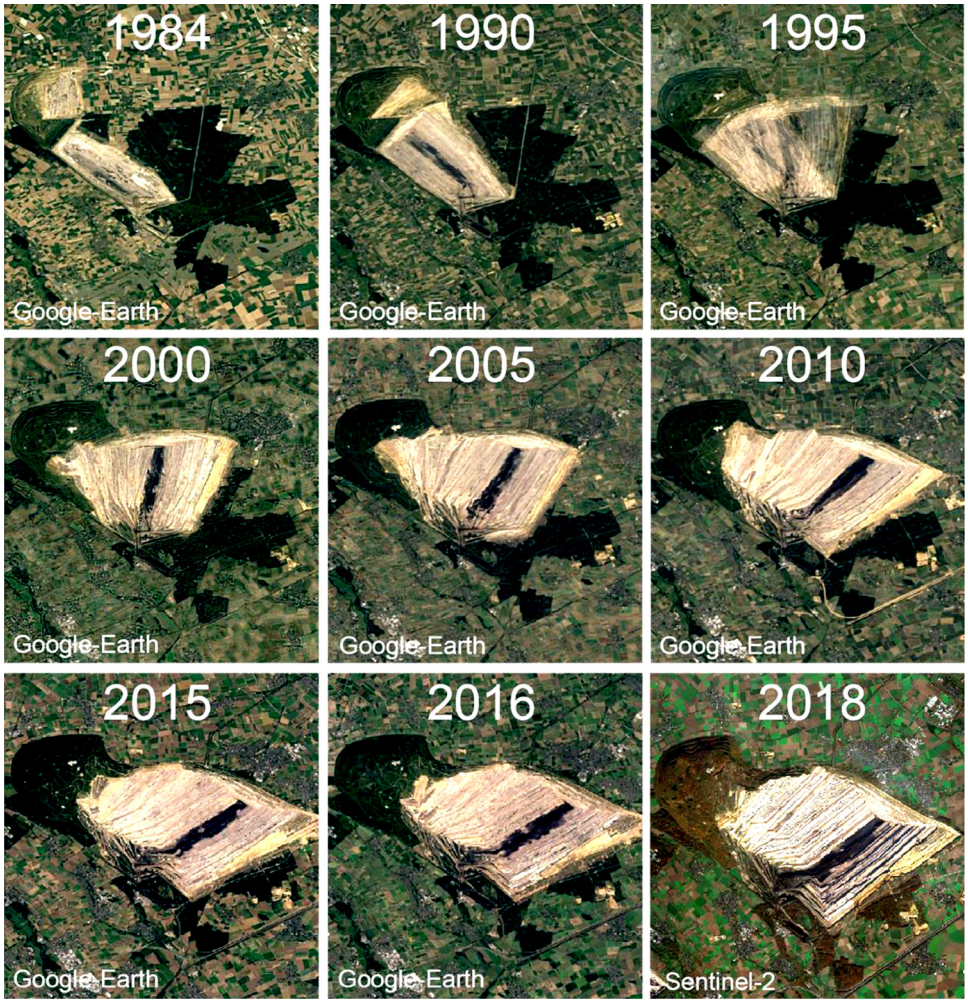

Fig. 2. Hambach mine and forest change over time.

Table 1
Parameters of SAR datasets in this study.

Sensor	SAR mode/geometry	Frequency band (wavelength)	Revisit time	Number of scenes	Incidence angle	Pixel spacing (rg×az)	Time period
S1A	IWS[a]/ascending	C band($\lambda = 5.6\,cm$)	12 days	29	37°	2.3 m×14.1 m	20171119-20181021
S1A	IWS[a]/descending	C band($\lambda = 5.6\,cm$)	12 days	42	47°	2.3 m×14.1 m	20170607-20181024
TSX	StripMap/descending	X band($\lambda = 3.1\,cm$)	11 days	27	35°	0.9 m×2.0 m	20170914-20180923

[a] IWS: Interferometric Wide Swath mode.

3. Methods

3.1. Interferogram generation

The new imaging mode of Terrain Observation by Progressive Scans SAR (TOPSAR) in Sentinel-1A/B satellites presents challenges to interferometric processing (De Zan and Monti Guarnieri, 2006). The Doppler variation in the azimuth direction related to the steering antenna on the satellite causes a phase jump between adjacent bursts. The co-registration accuracy needs to be on the order of 1/1000 of azimuth resolution to prevent this phase jump (Haghighi and Motagh, 2017). Thus, traditional image alignment fails with TOPSAR mode data. We applied the enhanced spectral diversity (ESD) method to align TOPS images (Yague-Martinez et al., 2016), which is implemented in GMT5SAR software (Sandwell et al., 2011; Xu et al., 2017). This method takes advantage of the phase differences in the overlapping areas between consecutive bursts to estimate the azimuth shift needed to suppress the phase mismatch. For TSX data, the conventional 2D image cross-correlation algorithm was used for image alignment (Sandwell et al., 2011). This alignment method uses a search window of 64 pixels. It can provide accurate co-registration even when the coherence is very low (near zero).

The interferograms are then generated by cross-multiplying, pixel by pixel, the first aligned images with the complex conjugate of the second images. We then used a 12-m TanDEM-X DEM to remove the topographic phase contribution and formed differential interferograms. To reduce speckle noise, the interferograms were decimated by 4×1 and 4×4 (rg × az) for S1A and TSX, respectively. This reduces the spatial resolution but improves the signal quality of pixels characterized by distributed scattering. A 200-m Gaussian filter was applied to limit the noise level in all the interferograms. The unwrapping procedure was implemented with Statistical-Cost, Network-Flow Algorithm for Phase Unwrapping (SNAPHU) software (Chen and Zebker, 2001). We used the GNU Parallel in the unwrapping program to reduce processing time

(Ole, 2011).

To limit phase decorrelation, spatial and temporal baselines below the chosen thresholds were applied to the selection of interferometric pairs. For S1A datasets, we used a 100-m baseline threshold and 50-day temporal threshold. For the TSX dataset, a 300-m baseline threshold and 50-day temporal threshold were used. Finally, we constructed 93, 135 and 61 interferograms from S1A ascending, S1A descending and TSX descending datasets, respectively. A baseline-time plot of interferograms for each SAR dataset can be found in the Supplementary Data (Figs. SD.1-SD.3), and the parameters of each interferogram are listed in Tables SD.4-SD.6.

3.2. Coherence-based SBAS methodology

To retrieve displacement time series, a method called coherence-based SBAS was adopted to analyse the stack of unwrapped interferograms. This method improves upon the traditional SBAS algorithm by incorporating coherence into the inverse problem (Tong and Schmidt, 2016). The pixels with low coherence are downweighted in the analysis. The coherence-based SBAS methodology is formulated as:

$$W\begin{bmatrix} 1 & 1 & 0 & \cdots & \beta B_{\perp,1} \\ 0 & 1 & 1 & \cdots & \beta B_{\perp,2} \\ \cdots & \cdots & \cdots & \cdots & \cdots \\ \frac{\rho}{\Delta t_1} & -\frac{\rho}{\Delta t_1} & 0 & \cdots & 0 \\ 0 & \frac{\rho}{\Delta t_2} & -\frac{\rho}{\Delta t_2} & \cdots & 0 \end{bmatrix}\begin{bmatrix} m_1 \\ m_2 \\ \cdots \\ m_s \\ h_{err} \end{bmatrix} = W\begin{bmatrix} d_1 \\ d_2 \\ \cdots \\ 0 \\ 0 \end{bmatrix} \quad (1)$$

where $W = diag\{\gamma_1, \gamma_2, \gamma_3, \cdots, \gamma_n\}$ is the weighted matrix, with γ_i indicating the coherence of the ith interferogram. $\beta = \frac{4\pi}{\lambda R \sin\theta}$, λ is the radar wavelength, R is the range distance from the radar to the centre of the interferogram, and θ is the incidence angle of the radar wave. $B_\perp$ is the perpendicular baseline. m_j is the incremental displacement for each SAR epoch, d_i is the line-of-sight (LOS) phase in the ith interferogram, and h_{err} is the DEM error. The value ρ is the smoothing factor. The design matrix has a size of $[n \times s + 1]$, where n is the number of interferograms and s is the number of temporal incremental displacements. The inverse problem is solved on a pixel-by-pixel basis with an iterative weighted least squares method. The deformation velocity was then computed by linear regression on the displacement time series.

The accuracy of InSAR results can be degraded by atmospheric phase delay. Because of the flat topography in this area, we did not expect a vertical stratification delay in the interferograms. Therefore, the atmospheric delay was estimated and removed by applying a common-point stacking method (Tymofyeyeva and Fialko, 2015). This method exploits the fact that the phase of interferograms sharing a common acquisition contains the same contribution from the atmosphere and uses an iterative approach to improve the estimates. The sufficient number of regularly acquired SAR images from S1A and TSX satellites helps improve the estimates of atmospheric noise in this area.

3.3. Decomposing LOS velocities into horizontal and vertical motions

One of the main objectives of this analysis is to investigate possible horizontal motions on/near the slope of the open pits to better understand the safety of the mines. However, InSAR can only measure 1-D deformation along the LOS direction, which hinders the interpretation and communication of InSAR measurements. It is possible to decompose the displacements into horizontal and vertical components by jointly analysing measurements from the ascending and descending interferograms (Fuhrmann and Garthwaite, 2019; Jin and Funning, 2017). Formally, the unit InSAR LOS vector, $\widehat{\boldsymbol{p}}$, is defined as the direction of motion (also referred to as "heading") of the SAR satellite, ϕ, and the radar incidence angle, θ:

$$\widehat{\boldsymbol{p}} = [p_x \quad p_y \quad p_z] = [-\cos\phi\sin\theta \quad \sin\phi\sin\theta \quad \cos\theta] \quad (2)$$

The displacement vector of the ground, $\boldsymbol{u} = [u_x \quad u_y \quad u_z]$, resolves into the LOS direction to give the range change, r, by scalar product, $r = \widehat{\boldsymbol{p}} \bullet \boldsymbol{u}$, where u_x, u_y, and u_z are the displacements in east-west (E-W), south-north (S-N) and vertical directions, respectively. With ascending and descending observations of range change, r_a and r_d, we can write two equations with the form of:

$$\begin{cases} r_a = \widehat{p}_a \bullet u \\ r_d = \widehat{p}_d \bullet u \end{cases} \quad (3)$$

In this equation, we have three unknowns (the three-dimensional displacements) and only two observations, so it is an ill-posed problem. Because of the near-polar trajectory and right-looking geometry of SAR satellites, InSAR lacks sensitivity to the motion in the south-north direction (i.e., $u_y = 0$). In this case, Equation (3) is solvable and can be written as a matrix problem:

$$\boldsymbol{r} = \mathbf{P}\boldsymbol{u}' \quad (4)$$

where $\boldsymbol{r} = [r_a \quad r_d]^T$, $\boldsymbol{u}' = [u_x \quad u_z]^T$, and $\mathbf{P} = \begin{bmatrix} -\cos\phi_a\sin\theta_a & \cos\theta_a \\ -\cos\phi_d\sin\theta_d & \cos\theta_d \end{bmatrix}$.

The solution to Equation (4) can be resolved by least squares:

$$\boldsymbol{u}' = [\mathbf{P}^T\mathbf{P}]^{-1}\mathbf{P}^T\boldsymbol{r} \quad (5)$$

4. Deformation results

The displacement time series and velocities over the three open-pit mines can be obtained after applying the coherence-based SBAS method to the stacked interferograms. In the results, we used a coherence threshold to mask out pixels with low coherence to prevent misinterpretation of patterns that resulted from phase decorrelation. Different SAR datasets operating at different wavelengths and spanning different time periods can have different sensitivities to phase decorrelation; thus, we used different coherence thresholds to select pixels for each SAR dataset. Specifically, pixels with temporally averaged coherence values smaller than 0.35, 0.3, and 0.25 were masked out in the S1A ascending, S1A descending and TSX results, respectively. The selection of reference pixels in space was based on statistical considerations concerning the average coherence (> 0.6) and on historical records of ground stability. In this study, we set the reference area to the urban area of Bergheim, approximately 7 km away to the east of the Hambach mine. Note that the same reference was set for the three SAR datasets to enable comparability. We also computed the root mean square (RMS) misfit from the linear regression of the displacement time series for each sensor, as shown in Supplementary Data (Figs. SD.7-9). Since the ground truth (such as levelling, GPS) was not available, we used the RMS to represent the uncertainty of the velocity. Areas with larger RMS indicate either larger errors (perhaps due to atmospheric or unwrapping errors) or nonlinear deformation. In Figs. SD.7-9, we can see that in the nondeforming areas, the RMS is homogenous and the magnitude is small. In the next three subsections, we show the InSAR LOS displacement results for each of the three open-pit mines.

4.1. Hambach open-pit mine

The LOS ground displacement velocity maps over the Hambach open-pit mine for each SAR dataset are shown and compared in Fig. 3. Both S1A ascending and descending maps indicate similar patterns overall. The velocity map derived from the TSX dataset looks generally smaller than that from the S1A dataset. Mismatches can be explained by the intrinsic differences in sensor/dataset properties (e.g., spatial resolution, revisit time, look angle and radar frequency). For example, a fast-moving displacement might be aliased in TSX interferograms due to its shorter wavelength.

Mining exploitation over the Hambach mine is progressing towards the S-E direction (as depicted in the optical image in Fig. 3d), and the

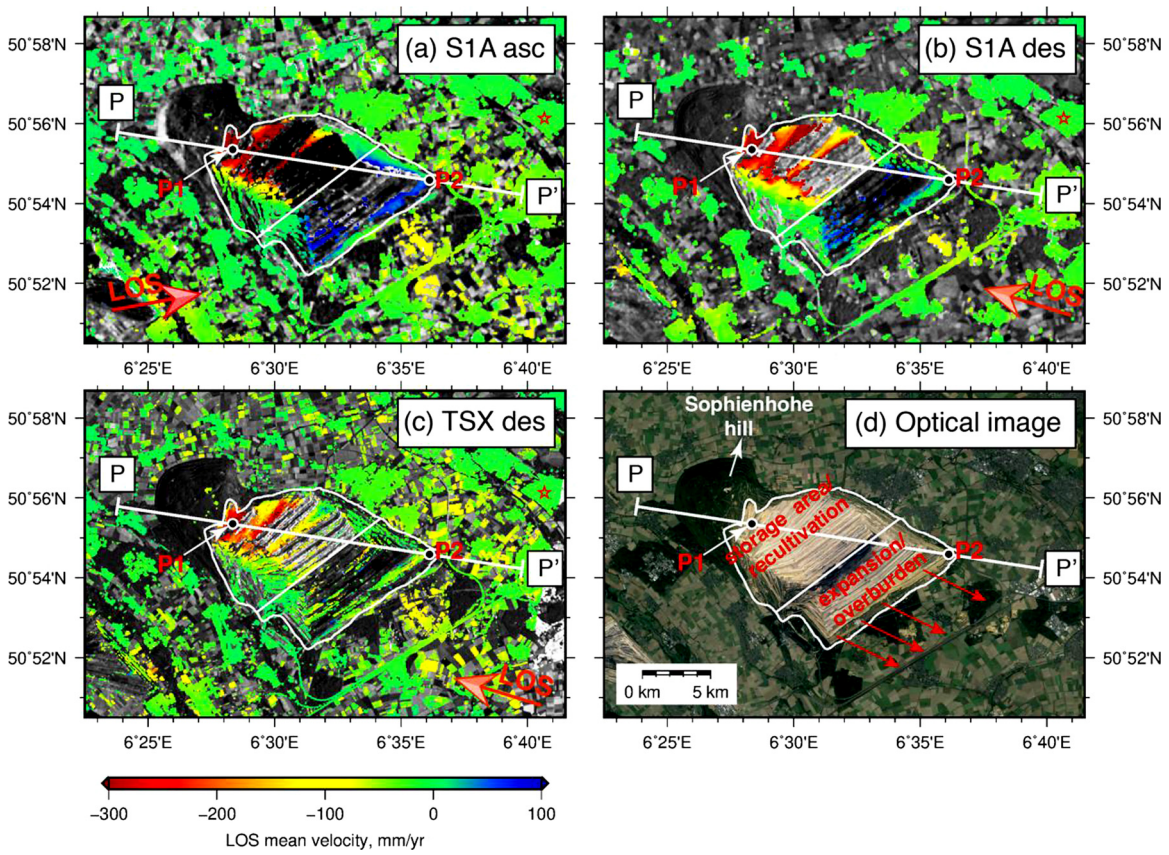

Fig. 3. LOS mean velocity maps over the Hambach open-pit mine. Background: Mean intensity image. (a) S1A ascending. (b) S1A descending. (c) TSX descending. (d) Optical image from Google Earth. The red star represents the reference point located in the stable area of Bergheim city. Black-filled circles (P1 and P2): Location of displacement time series shown in Fig. 5. A negative velocity means that the surface ground is moving away from the satellite, while a positive velocity represents that the ground is moving towards the satellite.

overburdens, i.e., loess, gravel and sand excavated from the working part, were moved to the western sector for reclamation purposes. The compaction process of the waste materials is the main contributor to the significant subsidence (maximum rate > 500 mm/yr) in the western area of the pit. Positive Line-of-sight (LOS) velocity, corresponding to either uplift or horizontal motion, was found in the eastern part of the Hambach mine, which might be related to excavation or construction activities in these areas.

The comparison of displacement velocities from the three SAR datasets along the P-P' profile is shown in Fig. 4. The negative velocity reaches -500 mm/yr at a distance of ~5.2 km along the profile in the western part of the pit, while the positive rate reaches +200 mm/yr at ~12.9 km in the eastern part. The LOS displacement time series at two selected points (P1 and P2) is displayed in Fig. 5. Pixels within a circular area with a radius of 50 m were selected, and the average displacement was computed. The displacement time series between different datasets were referenced to the same date, and offsets were shifted for comparison. The standard deviation of displacements for the selected pixels was also computed and used as an error bound at every SAR scene. The error bounds account primarily for uncorrelated spatial noise in the derived displacement time series (e.g., decorrelation and local unwrapping errors) by assuming that nearby pixels have similar displacement behaviour. Steady land subsidence was found at P1 in the western part of the mine, and the close agreement between ascending

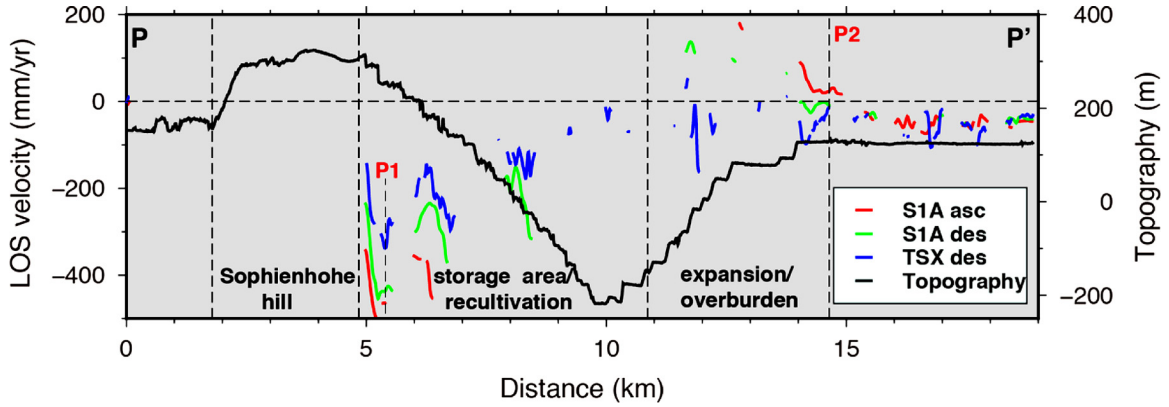

Fig. 4. The A-A' LOS velocity profile. The profile location is given in Figure 3. The gaps occur where phase noise is significant and the pixel is discarded. The topography profile (black line) is extracted from the TanDEM-X 12-m DEM.

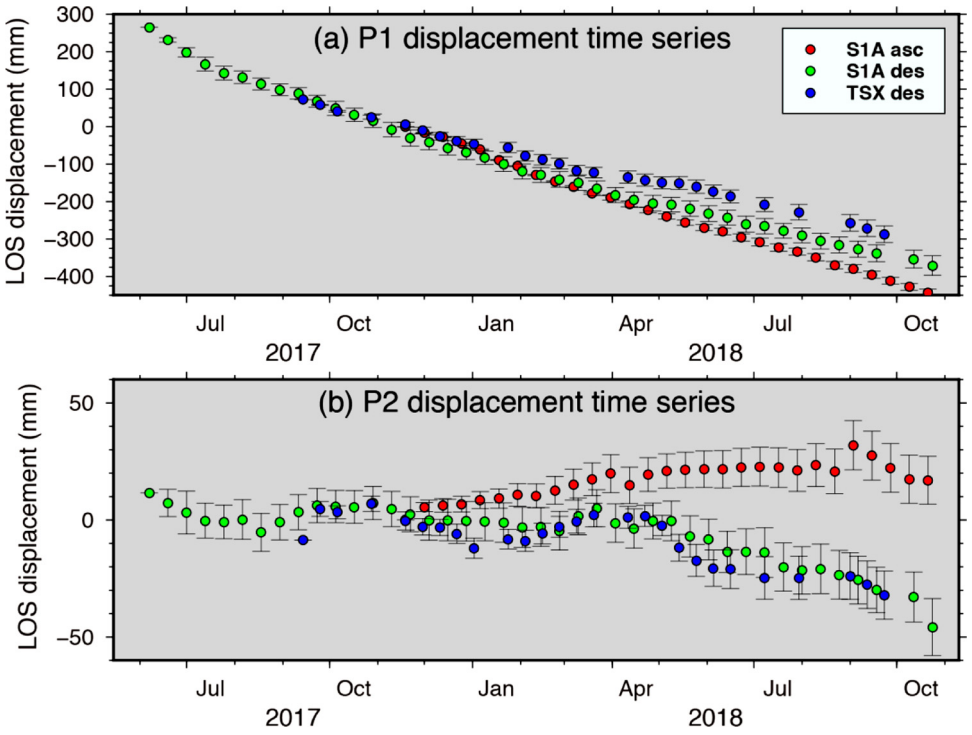

Fig. 5. LOS displacement time series at the P1 and P2 locations in the Hambach mine.

and descending datasets suggests that the displacement mainly occurred in the vertical direction. At point P2, consistent results were found between descending datasets in which the ground was moving away from the satellite, but an opposite displacement behaviour from the S1A ascending dataset was also noted. These measurements from different viewing geometries indicate the existence of horizontal movement in the eastern part of the mine.

4.2. Garzweiler open-pit mine

The LOS velocity maps over the Garzweiler mine are shown in Fig. 6. This mine is being excavated westward (indicated as the red arrows in Fig. 6d), and the overburden is primarily used to refill the eastern areas when the mine operation is completed. Similar to the displacement pattern in the Hambach mine, the reclamation areas in the east suffered from steady subsidence (maximum rate > 380 mm/yr), while the areas near the active working part in the west are undergoing LOS uplift.

The displacement time series at two selected points (P3 and P4) in the Garzweiler mine is displayed in Fig. 7. The displacement in the storage area (at P3) shows a linear trend, and the results between the three SAR datasets are in good agreement, suggesting that this location is mainly affected by subsidence. In the expansion area (at P4), the displacement between the ascending and descending datasets shows the opposite trend, indicating that this part of the structure could be affected by horizontal displacement.

4.3. Inden open-pit mine

The LOS velocity maps over the Inden mine are shown in Fig. 8. This mine is expanding to the southeast (Fig. 8d), and these locations are undergoing LOS uplift. Similar to the Hambach and Garzweiler mines, the recultivated area in the northwest of the pit is suffering from land subsidence. When the mine is exhausted, the Inden coalfield will not be backfilled with overburden. Instead, a large residual lake is planned for this area. The stability of the surrounding ground and the surface slope of the mine void must be considered. As shown in Fig. 8, the maximum rate of land subsidence in the western part of the mine reach ~310 mm/yr, while the maximum rate of land uplift in the eastern part are approximately 80 mm/yr.

We also plotted and compared the displacement time series at two selected points (P5 and P6) in the Inden mine, as shown in Fig. 9. Again, no significant differences are observed between each of the three SAR datasets in the recultivated areas at P5, while an opposite displacement behaviour is revealed between the ascending and descending geometries near the areas under production work at P6. From the displacement time series, we found that the land subsidence in the storage areas of these open-pit mines is linear and primarily occurs in the vertical direction. However, the ground displacements in the area near the active working parts of the mines exhibit horizontal motion and a more complex behaviour (fluctuation in time).

5. Discussion

5.1. DEM errors due to topographical changes

Due to excavation and reclamation activities, the surface topography over open-pit mining areas is continuously changing. The changed surface topography can result in phase residuals in the differential interferograms when the SRTM DEM is used for the removal of the phase contribution from the topography. By comparing the DEM data acquired at different times, we can analyse the changes in the surface topography. Fig. 10 compares the topography between the TanDEM-X 12-m DEM acquired in 2013 and the SRTM 30-m DEM acquired in 2000. The positive values in Fig. 10c correspond to reclamation areas, and the negative values correspond to excavation areas.

Fig. 11 shows some examples of differential interferograms with different perpendicular baselines (minimum = -1 m, moderate = -63 m, maximum = 99 m) over the three open-pit mines. Examples of interferograms from S1A and TSX descending datasets are shown in the Supplementary Data (Figs. SD.10 and SD.11). Fringes can be clearly observed in the interferograms, with one fringe corresponding to half the radar wavelength (2.8 cm for S1A, 1.5 cm for TSX) of ground

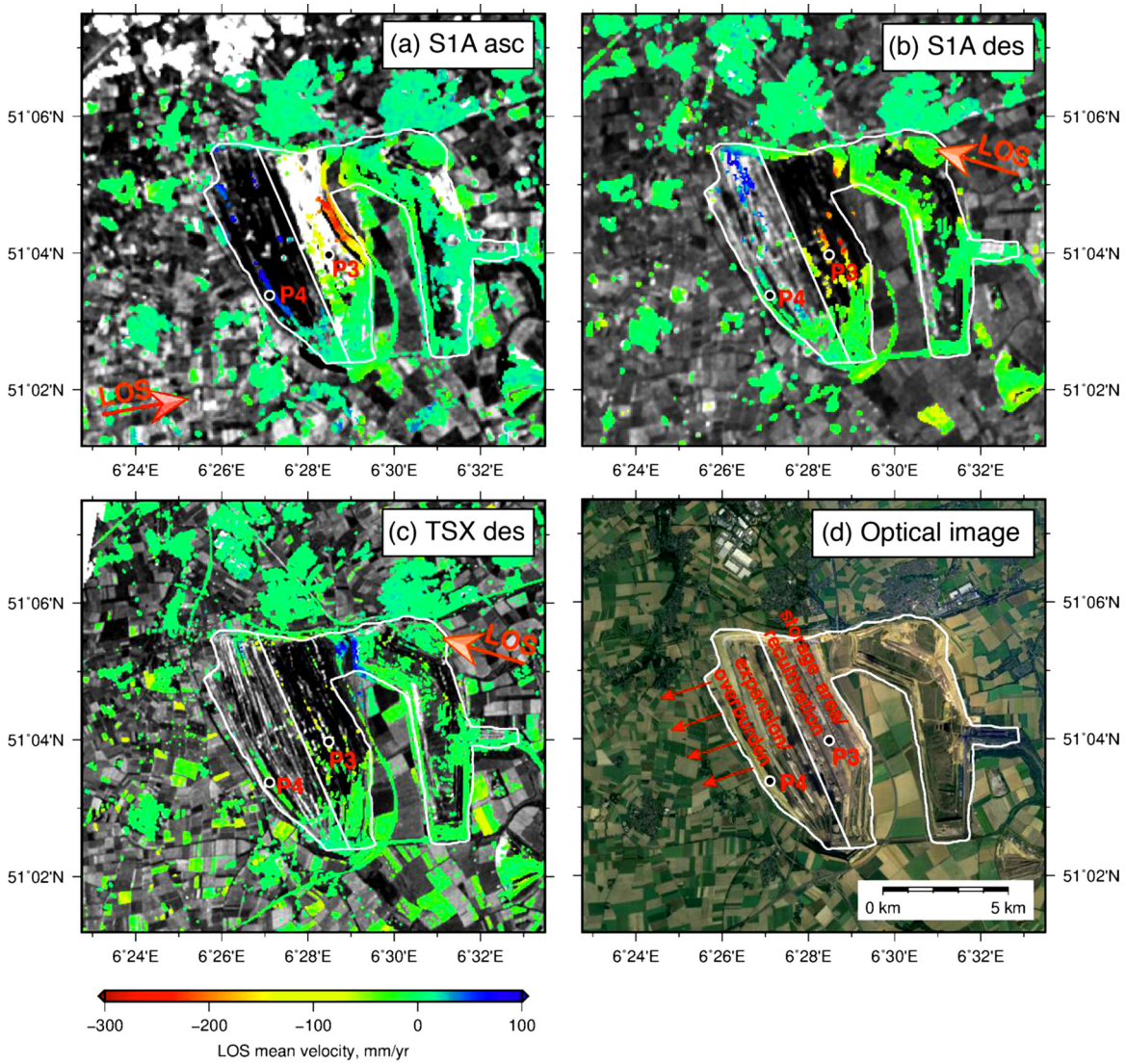

Fig. 6. LOS mean velocity maps over the Garzweiler open-pit mine. Black-filled circles (P3 and P4): Location of displacement time series shown in Fig. 7.

motion in the LOS direction. These fringes are mostly induced by ground deformation but could be related to topographic errors, even though the resolution and accuracy of the TanDEM-X DEM used for topographic phase removal are high. This is because the DEM was produced several years before the SAR acquisitions, and topographical changes due to ongoing production works may result in phase residuals (Haghighi and Motagh, 2017).

The residual topographic error is baseline-dependent and can be expressed as $\Delta\varnothing_h = \beta B_\perp h_{err}$. The height of ambiguity (HoA) is used to quantify the phase sensitivity to topographic effects. The HoA is defined as the elevation difference that generates an interferometric phase change of 2π after interferogram flattening and is expressed as:

$$HoA = \frac{\lambda R \sin\theta}{2B_\perp} \tag{6}$$

The smaller the value of $B_\perp$ is, the higher the HoA, i.e., the lower sensitivity to the topographic error. As discussed in Section 3.1, we constrained the interferometric pairs with $B_\perp < 100$ m for the S1A dataset and < 300 m for the TSX dataset. This severely restrained the topographic phase residuals in the interferograms. We computed the HoA values for all interferograms used in this study, which are listed in Supplementary Data (Tables SD.4-SD.6). Taking the case of the interferogram with $B_\perp = 99\,m$ in Fig. 11 (the largest $B_\perp$ among all the interferograms), which corresponds to the smallest HoA of ~135 m. This will cause a topographic phase residual $\Delta\varnothing_h \approx 0.23\,rad$ (equivalent to ~1 mm displacement) according to the nominal accuracy of the TanDEM-X 12-m DEM (relative vertical accuracy is 4 m for areas with slope > 20%) (Wessel et al., 2018). For TSX interferograms, the largest $B_\perp$ is ~299 m (the interferogram shown in Fig. SD.11 in the Supplementary Data), corresponding to the smallest HoA of ~19 m, leading to a topographic phase residual of $\Delta\varnothing_h \approx 1.3\,rad$ (~5.7 mm displacement). Interferograms with smaller $B_\perp$ values will have lower sensitivity to DEM errors. Therefore, the effects of DEM errors on the differential interferograms formed with a small perpendicular baseline in our study are very small.

5.2. Investigating slope instability over the Hambach mine

By jointly analysing the results from ascending and descending geometries, we can tell more about the orientation of the deformation. We applied the decomposition as described in Section 3.3 to the S1A ascending and descending LOS results to find the E-W and vertical displacement patterns for the three open-pit mines. The result of the velocity decomposition over the Hambach mine is shown on the map view in Fig. 12, and the decomposition results over the Garzweiler and Inden mines are shown in the Supplementary Data (Figures SD.12 and

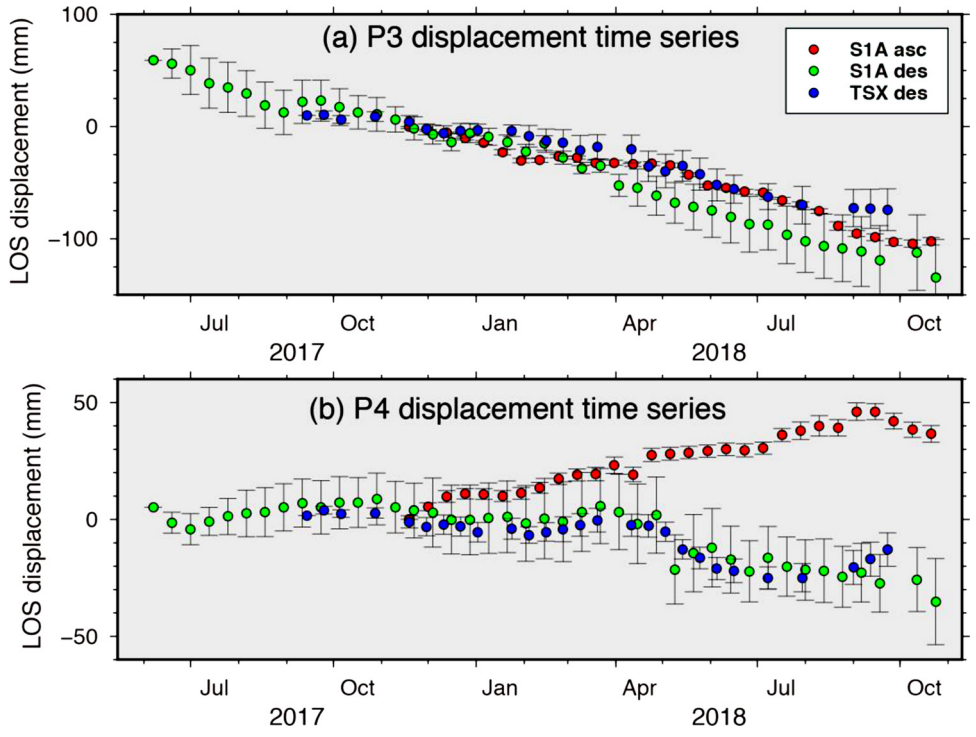

Fig. 7. Displacement time series at the P3 and P4 locations in the Garzweiler mine.

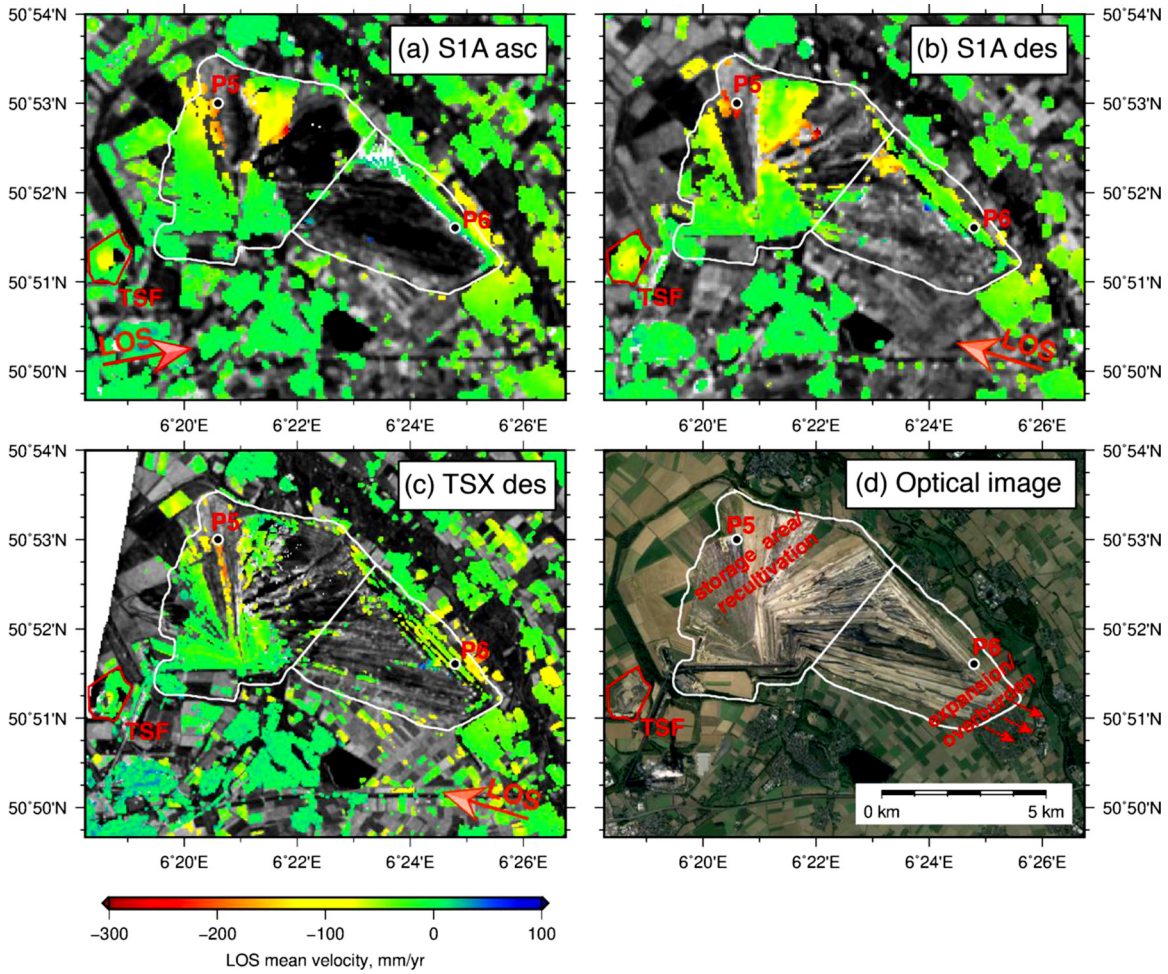

Fig. 8. LOS mean velocity maps over the Inden mine. Black-filled circles (P5 and P6): Location of displacement time series shown in Fig. 9. The red polygon in the southwest of the Inden mine represents a tailing storage facility (TSF), which we will discuss in Section 5.3.

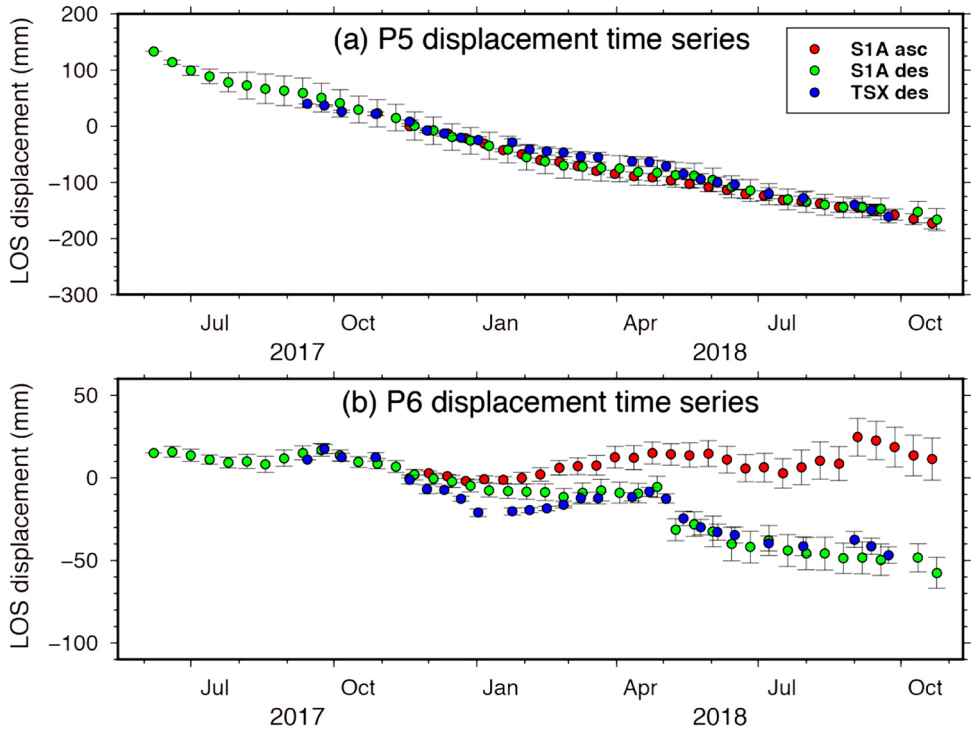

Fig. 9. Displacement time series at the P5 and P6 locations in the Inden mine.

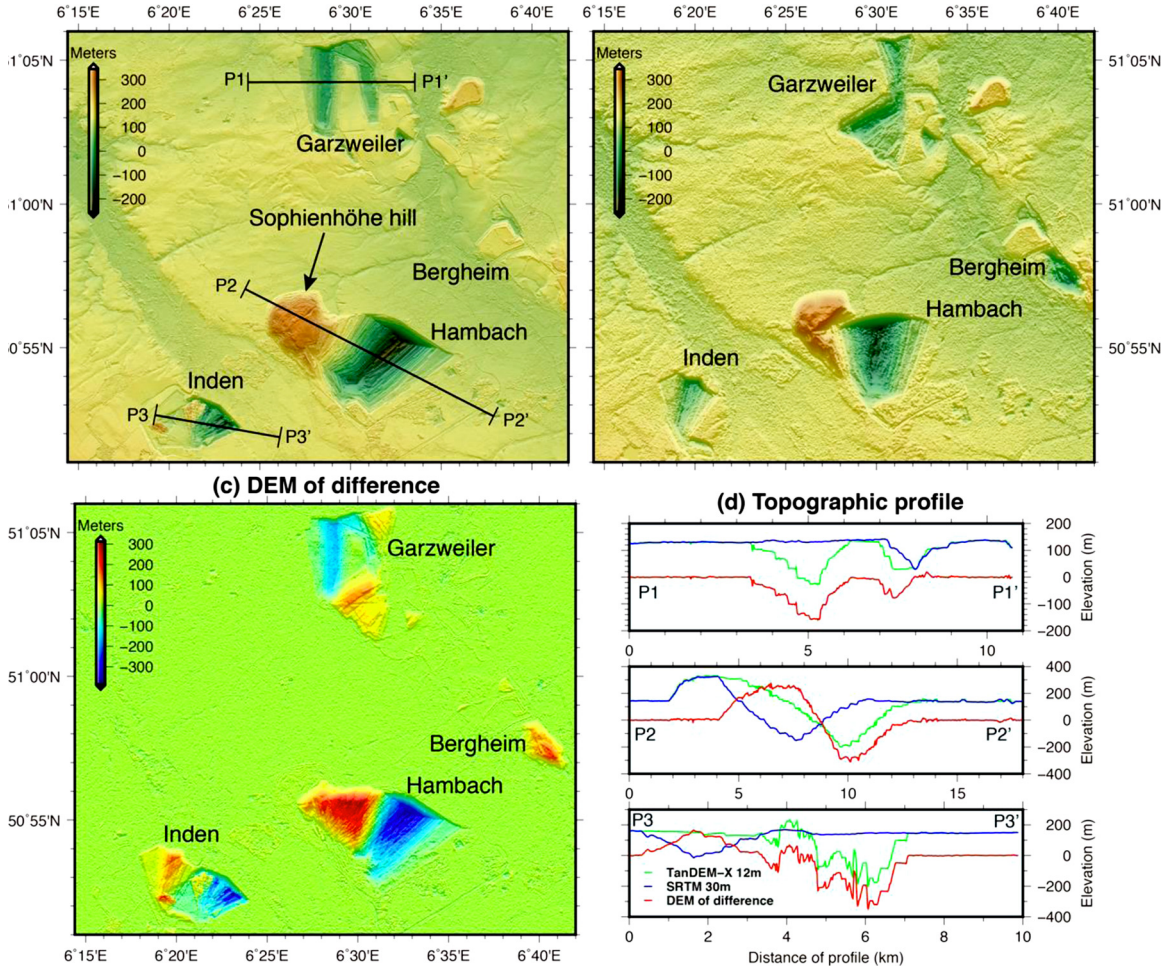

Fig. 10. Comparison between TanDEM-X and SRTM. (a) Topography from TanDEM-X 12-m, with indication of topographic profile locations. (b) Topography from SRTM 30 m. (c) Differences in the DEM (TanDEM-X minus SRTM). (d) Topographic profiles.

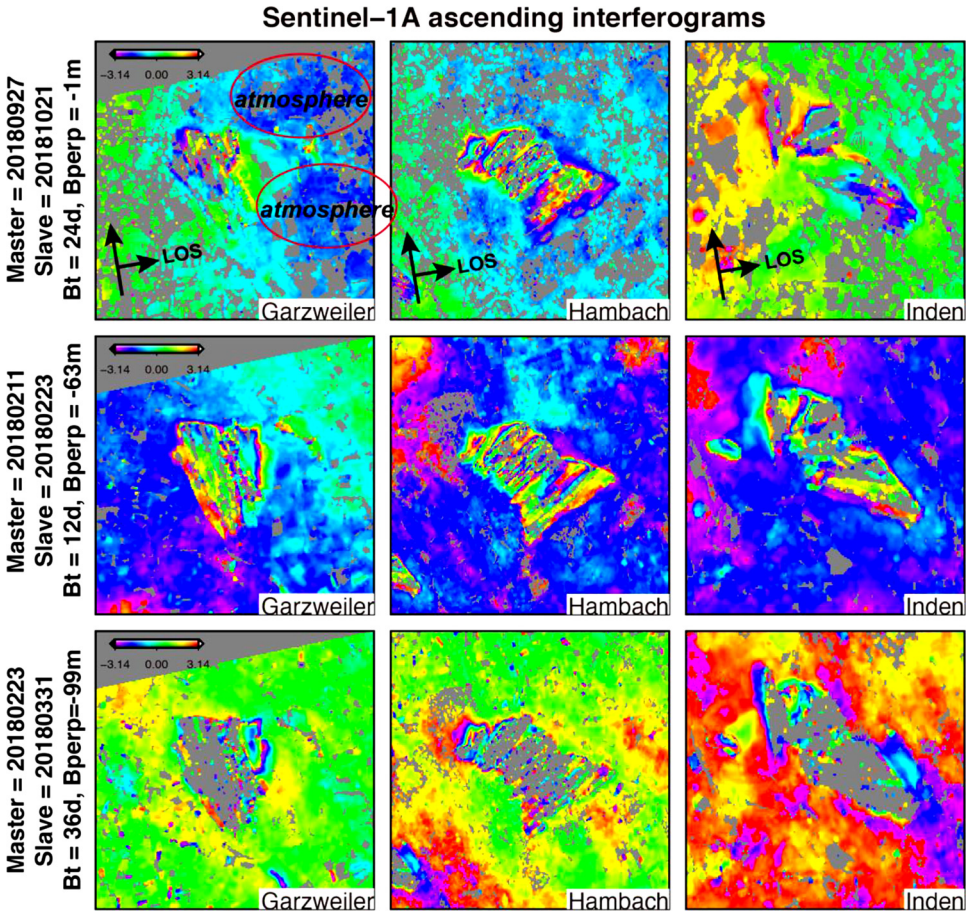

Fig. 11. Example of differential interferograms with different perpendicular baselines from the S1A ascending dataset. The interferograms were masked with a coherence threshold of 0.2.

SD.13). In the following, we will discuss the case of the Hambach open-pit mine.

The main characteristic of this mine is that the slope is extremely steep and high (with a present height of ~255 m), which is prone to slope failure endangering human safety and property. From the surface to the bottom of the pit, many different geological layers are exposed due to the variability of geotechnical conditions along the slope (Hu, 2013). Slope instability assessment and failure prediction are critical to ensure the secure operation of the mine. We analysed the spatial distribution of horizontal deformation data with respect to the slope structure and slope angle map of the mine, as shown in Fig. 13. In Fig. 13, we can see that eastward or westward displacement in the horizontal direction was detected, depending on the location along the structure of the pits. The horizontal movements are mainly located on the benches with slope angles larger than 25 degrees (Fig. 13b).

The 2D displacement vectors (horizontal and vertical) can be visually combined on profile P-P', as shown in Fig. 14. The transition of the movement direction following the slope orientation is visible along the profile. The slope descending towards the east exhibits eastward movement with a maximum rate of ~120 mm/yr in the western part of

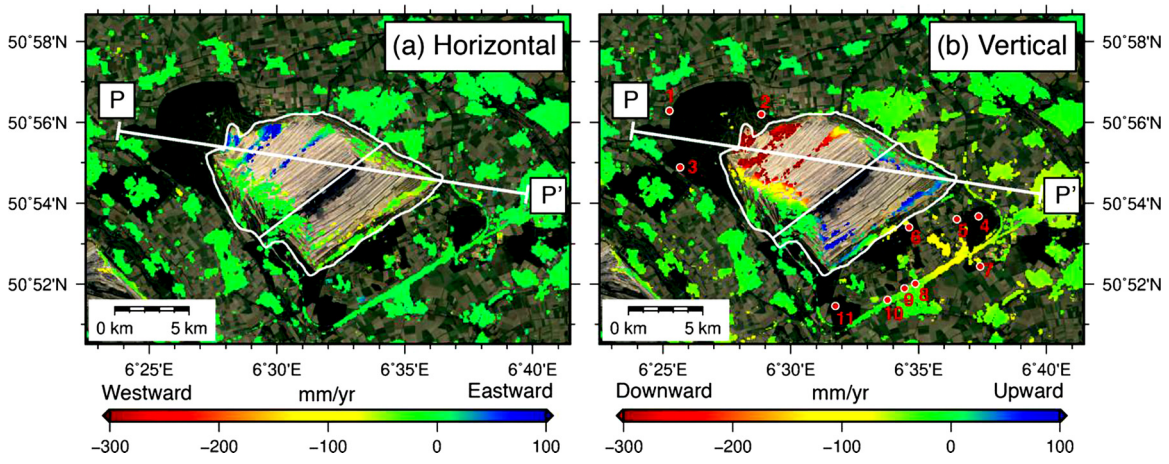

Fig. 12. Decomposition of the horizontal (left) and vertical (right) components for the velocities by a combination of S1A ascending and descending geometries over the Hambach mine. The red points in (b) indicate the location of the water wells used for analysis in Section 5.5.

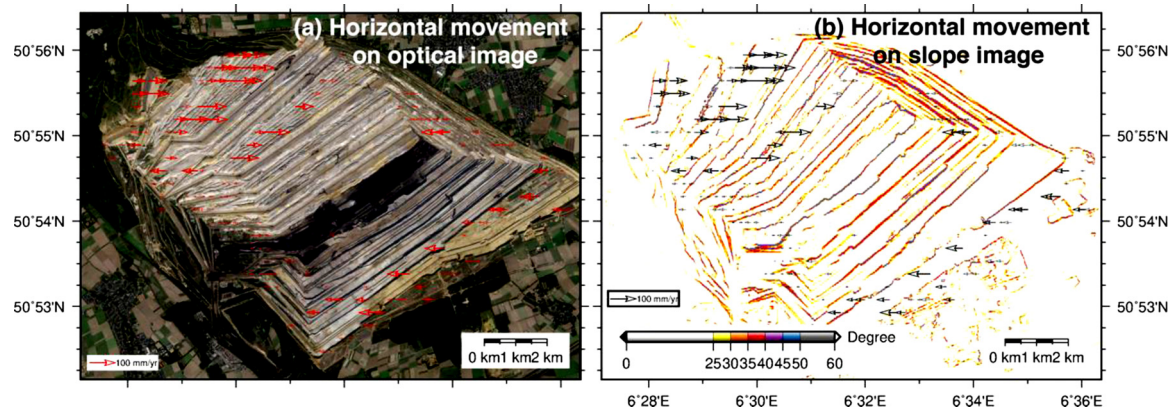

Fig. 13. InSAR horizontal movement of the Hambach open-pit mine superimposed on (a) the optical image and (b) the slope angle map. Arrows correspond to horizontal motion, with the length of the arrow corresponding to the displacement magnitude. The slope angle map is computed by using the TanDEM-X 12-m DEM.

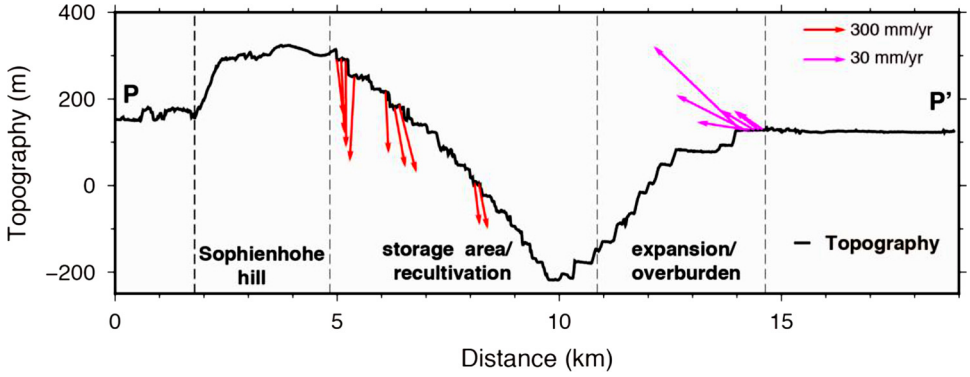

Fig. 14. The 2D displacement vectors (horizontal and vertical) from the combination of S1A result in ascending and descending geometries. The location of profile P-P' can be found in Fig. 12. Due to large differences in the magnitude of displacement in different locations, we used different scales for the vectors in the western (red) and eastern (magenta) parts of the mine. The topography profile (black line) is extracted from the TanDEM-X 12-m DEM.

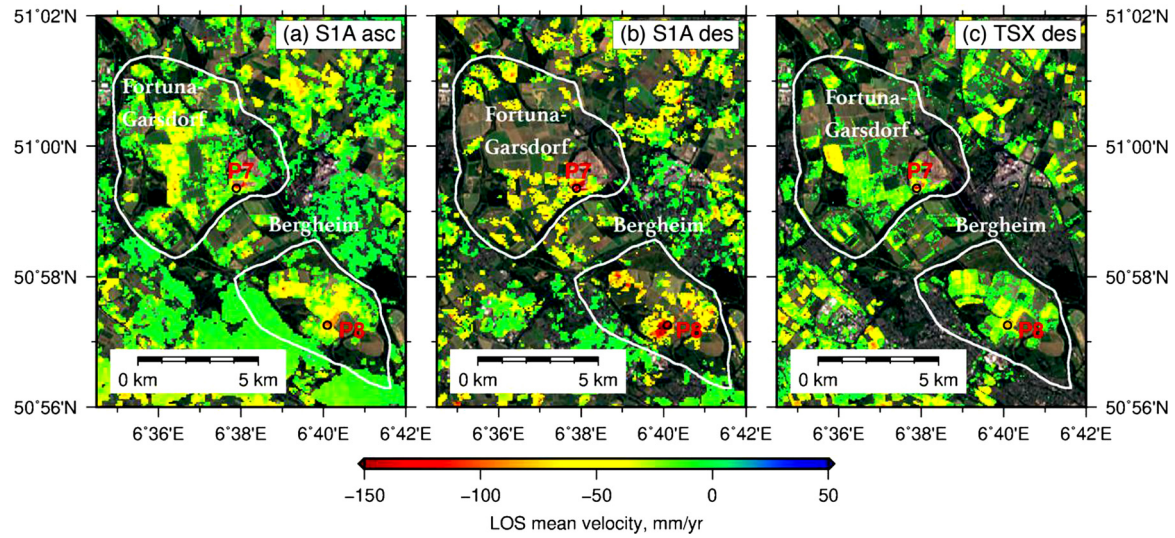

Fig. 15. The LOS subsidence rate over Fortuna-Garsdorf and Bergheim reclaimed sites (for the locations of the two mines, see Fig. 1). Black circles (P7 and P8): Location of time series shown in Fig. 16.

the pit. When the slope becomes oriented towards the west, the horizontal displacement becomes logically westward in the eastern part of the pit. The westward motion rate can reach ~60 mm/yr. The magnitude of horizontal movement appears reasonably comparable in the western and eastern parts of the pit, but the magnitude of land subsidence in the west is nearly 10 times greater than the land uplift in the east.

High horizontal deformation rates were detected over the Hambach mine but may not represent any hazard since they are expected displacements in metres of magnitude for the areas reclaimed by loose materials. We inferred that this involves only the superficial soil material and not the bedrock. Actually, both deformation and tolerated collapse are welcome in an open pit, as they do not cause fatalities or damage but allow the bench slope to stabilize itself. For this reason, the main concern in an open pit is whole bench slope stability and several conjunct bench slope stabilities that are characteristic of large-scale failure and high risk (Hu, 2013).

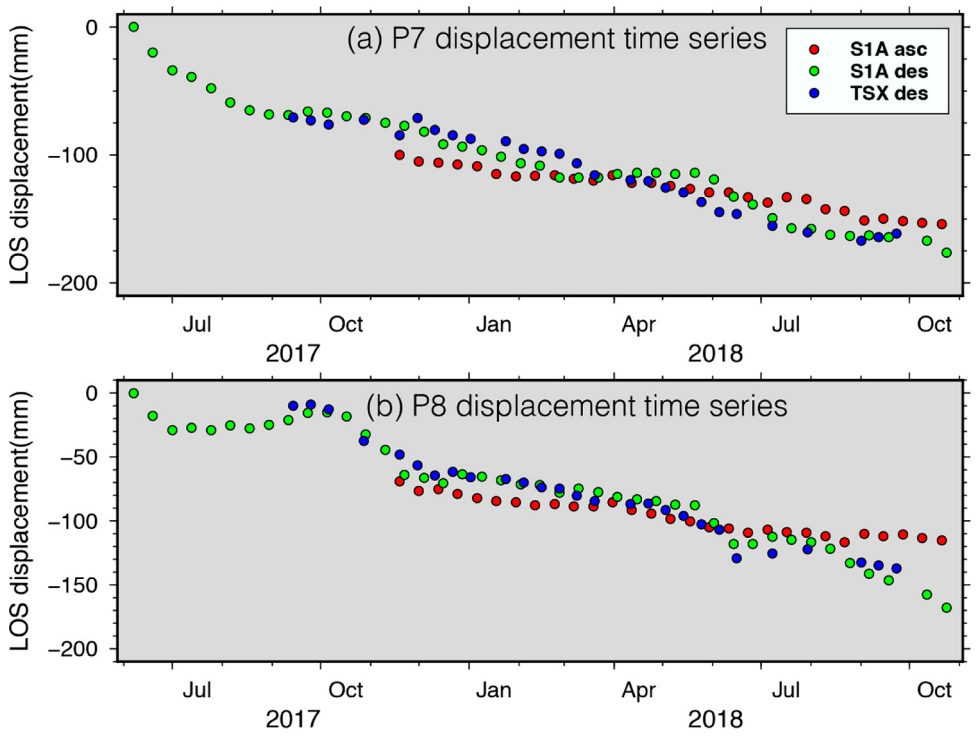

Fig. 16. LOS displacement time series at the location of P7 and P8 over Fortuna-Garsdorf and Bergheim reclaimed sites.

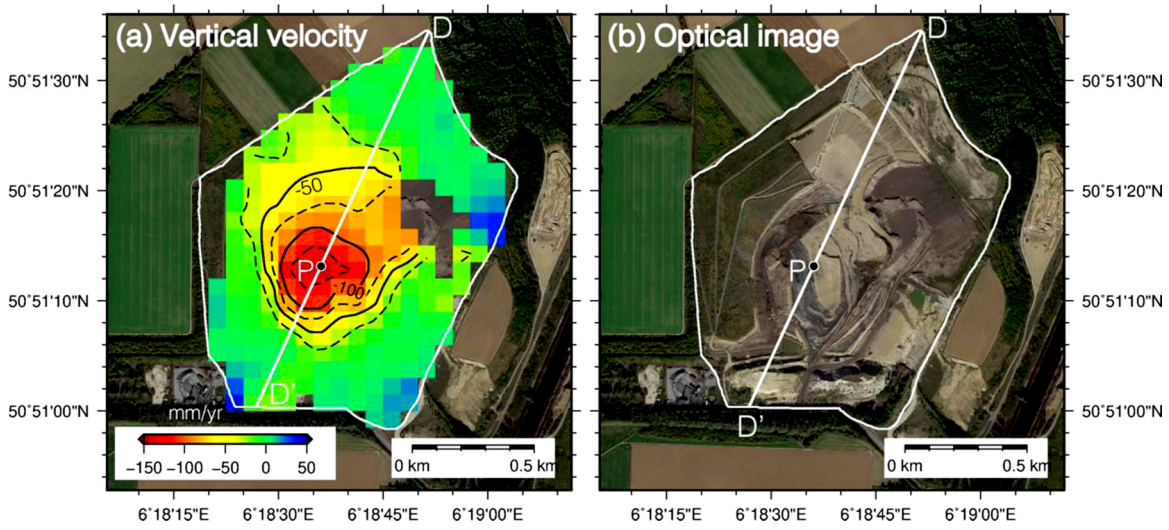

Fig. 17. Deformation rate in the vertical direction over a TSF located in the southwest of the Inden mine. The white straight line indicates the location of the D-D' profile. The black-filled circle P indicates the location with the maximum velocity along the D-D' profile.

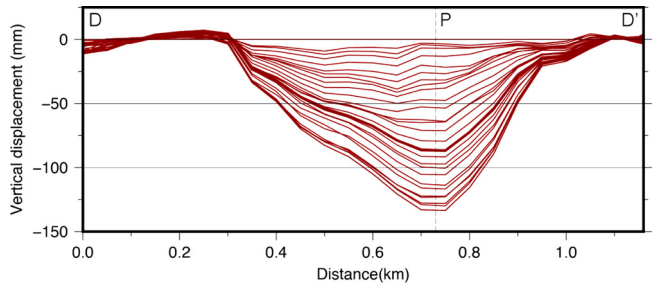

Fig. 18. Evolution of vertical displacement along the D-D' profile. Each profile represents an isochronous cumulative vertical displacement line. The vertical dashed line indicates the location of point P shown in Fig. 17.

5.3. Land subsidence over former open-pit mines

Reclamation involves a number of activities aimed at restoring mined land to an acceptable environmental state and to productive use after the completion of mining operations (Alves Dias et al., 2018). Land subsidence monitoring is one of the activities required to assess the effectiveness of reclamation measures. The artificial ground surfaces reclaimed with waste materials such as loess, gravel and sand are prone to land subsidence related to the compaction process.

Former open-pit mines in the eastern part of the Rhenish lignite mining district (the open-pit mines Fortuna-Garsdorf and Bergheim; see the locations in Fig. 1) were recultivated and rehabilitated. After the mining activities were completed, the two open pits were filled with overburden from other open-pit mines in the region. Now, the two areas are used for agriculture. The historical evolution of the two mines can

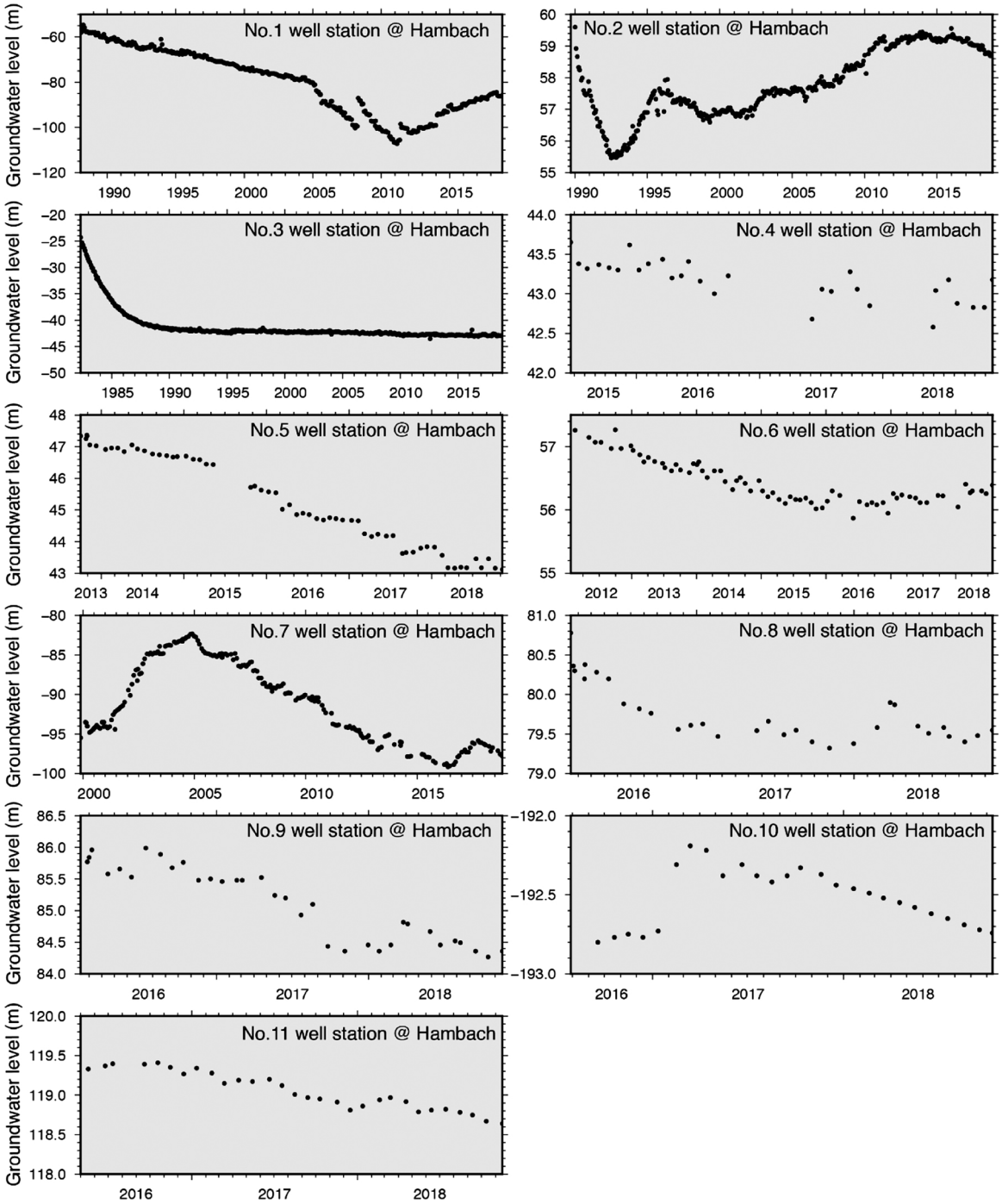

Fig. 19. The groundwater level change over the Hambach mine. For the locations of water wells, refer to Fig. 12b.

be viewed in the video in the Supplementary Data. The maps of subsiding rates over the two reclaimed sites are shown in Fig. 15. Despite temporal decorrelation caused by fast changes in the agricultural field our SBAB analysis detected enough coherent pixels in these regions. In the P7 and P8 locations (black circles), subsidence reached a maximum rate of 150 mm/yr. A reasonable consistency between the three SAR datasets was found on the LOS displacement time series at the two points in Fig. 16. No significant variation in the subsidence rate is observed during the monitoring period. This indicates that the land subsidence is irreversible, implying that the land reclaimed with loose materials is still undergoing a consolidation process.

5.4. Displacement over tailing storage facility (TSF)

Owing to the extraction of lignite, the predominantly sandy overburden of tertiary and quaternary age material has to be excavated and deposited (Lenk and Wisotzky, 2011). A TSF is a structure built for storing the overburden material and water from mining operations. This structure accumulates debris material where ground movement is a very frequent phenomenon that could cause untold tragedies, including catastrophic loss of property and life and damage to infrastructure and the environment. Thus, the safety of TSFs near lignite mines is a source of great concern.

A TSF located in the southwest of the Inden mine (the location can be found in Fig. 8) was built for storing waste materials (ground-up rock

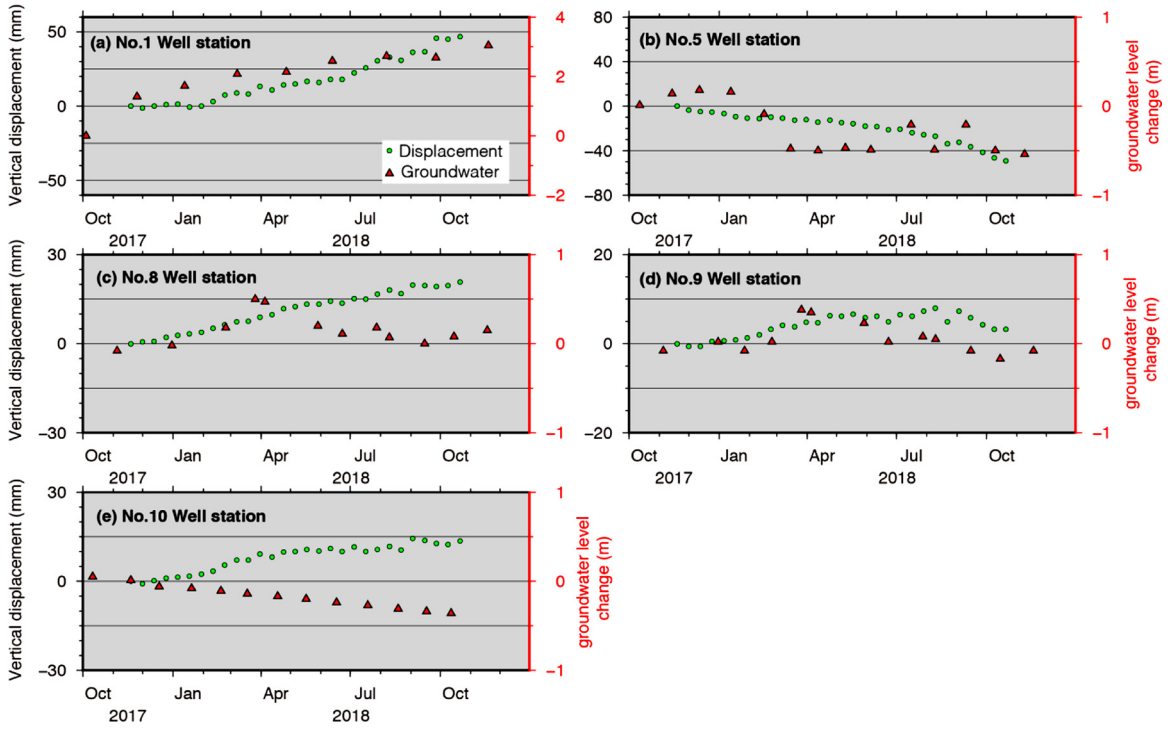

Fig. 20. Groundwater level changes against vertical ground displacement derived from InSAR. For the location of these wells, refer to Fig. 12b.

or sand) extracted from the Inden mine. A subsidence funnel was formed with a maximum rate up to 140 mm/yr, as shown in Fig. 17a. The historical evolution of ground displacement along the D-D' profile is shown in Fig. 18, with the trough at the location of point P (see the point location in Fig. 17a). Each profile represents an isochronous cumulative vertical displacement line. Compaction processes of the unconsolidated material accumulated in the tailing storage areas are responsible for the vertical ground deformation.

5.5. The link between displacement and groundwater level

In this section, the ground displacement around the Hambach mine was analysed with respect to groundwater withdrawal. The top strata in the Rhenish coalfield are loose, so the lignite can only be extracted in open-pit mines (Lenk and Wisotzky, 2011). For this reason, the groundwater table must be lowered, i.e., pumped to the surface and piped away. Several hundred drainage wells around the mines and an extensive network of pipelines were constructed to remove 600 million m^3 of water from the Rhenish coalfield (Hu, 2013). The locations of water wells around the Hambach open-pit mines are indicated as the red points on the rate maps in Fig. 12b.

Long-term (1960-2018) groundwater level changes for those water wells are shown in Fig. 19. Water wells 1, 2 and 3 are located in the reclamation area around Sophienhöhe hill. For well station 1, the water level sharply decreased by ~53 m from 1990 to 2010 and rose by ~22 m from 2011 to 2018. The groundwater level at water wells 2 and 3 decreased during the 1980s-1990s before the mine was excavated, but it rose again at well 2 after 1993; however, at well station 3, the groundwater level remained stable at its lowest level, even after the completion of mining activities. The other water wells (No. 4-No. 11) are located east of the Hambach mine and are near the active working part of the mine. Dewatering at these well stations facilitated the excavation works, leading to a reduction of the groundwater table (maximum reduction of ~5 m at well station 5).

To identify the correlation between the groundwater level and ground deformation at each water well, the land displacement and groundwater level time series were analysed. Fig. 20 illustrates the time series of ground displacement in the vertical direction versus changes in groundwater level at the five water wells around the Hambach mine. Land uplift was detected at well station 1 due to a rising groundwater table, as shown in Fig. 20a. Extensive groundwater extraction has caused land subsidence in the surrounding area; see the No. 5 well station in Fig. 20b. However, land uplift with a magnitude of 10-20 mm was found at stations 8, 9 and 10. This is due to aquifer unit rebound following the slight rerise of groundwater level from October 2017 to April 2018 at stations 8 and 9. We observed a negative correlation between groundwater table change and ground deformation at the No. 10 well station, as shown in Fig. 20e, i.e., the No. 10 well station. The groundwater level continuously declined while the land was uplifted. Generally, we can infer that the groundwater level was lowered by artificial pumping in the surrounding areas of the mines, which resulted in ground deformation.

6. Conclusion

Ground stability is one of the most critical issues when dealing with safety in open-pit mines. In this paper, ground surface displacements around three active open-pit mines (Hambach, Garzweiler and Inden) in the Rhenish coalfields of Germany were investigated by means of a space-borne InSAR time series method. Due to the continuous change in topography, we used a coherence-based SBAS algorithm to jointly estimate displacements and DEM errors over the active open-pit mines. We also showed that the results from complementary SAR geometries could be combined to calculate two-dimensional displacements for analysing the slope instability over the pits. Ground instabilities, including horizontal and vertical movements, were found on the slopes of all three open pits, indicating potential problems. A comparison with all potentially available in situ measurements in our further work would be of interest to fully assess the geotechnical risk of the mines. Significant land subsidence was found in the storage/recultivation areas, and the main reason was the compaction process of the unconsolidated soil materials. Our work also indicates that the ground subsidence in the areas surrounding the mines is related to groundwater pumping for the purpose of lignite extraction.

The results of InSAR ground deformation measurements over three active open-pit mines show the potential of using InSAR techniques to upscale the monitoring of slope instability. As opposed to other geodetic tools, InSAR provides measurements at a large scale with high spatial resolution. This is of interest in the mining industry, where the field conditions are difficult and in situ instrumentation networks are challenging and expensive to set up. With the launch of Sentinel-1A/B satellites, the acquisition rate decreased to six days, and the large illuminated tracks (200 km wide) make the Sentinel-1A/B constellation an attractive source of data to study ground deformation over open-pit mines. With the high spatial resolution images from the TerraSAR-X satellite, InSAR further provides ground displacement information in more detail. Such displacement data are not only useful for the identification of unstable areas but also applicable to identify time series indicating a forthcoming landslide and theoretically allow for slope failure forecasting, which is at least helpful for decision making on risk management. However, it is fair to point out that the limitation of the InSAR technique is that it typically requires a large number of multi-temporal images for processing, which may conflict with the need for rapid responses in an early warning system framework.

CRediT authorship contribution statement

Wei Tang: Conceptualization, Methodology, Software, Writing - original draft. **Mahdi Motagh:** Data curation, Writing - review & editing, Supervision. **Wei Zhan:** Vizualization.

Declaration of Competing Interest

The authors declare that they have no known competing financial interests or personal relationships that could have appeared to influence the work reported in this paper.

Acknowledgments

The first author gratefully acknowledges financial support from Sino-German (CSC-German) postdoc scholarship program to pursue one year of research at GFZ. This research was also partially supported by the National Key R & D Program of China (Grant number 2018YFC1503606), funded by the Ministry of Science and Technology of the People's Republic of China, by Open Fund of State Laboratory of Information Engineering in Surveying, Mapping and Remote Sensing, Wuhan University (Grant No. 17R03) and by the Fundamental Research Funds for the Central Universities (Grant No. 2020YQDC06). TerraSAR-X data are copyright German Aerospace Agency (DLR) and were provided under the proposal motagh_GEO1371. The Copernicus Sentinel data were provided by ESA. For groundwater data, we acknowledge Anke Boockmeyer from Landesamt für Natur, Umwelt und Verbraucherschutz NRW. Some of the figures were generated using Generic Mapping Tools (Wessel et al., 2019).

Appendix A. Supplementary data

Supplementary material related to this article can be found, in the online version, at doi:https://doi.org/10.1016/j.jag.2020.102217.

References

Alves Dias, P., Kanellopoulos, K., Medarac, H., Kapetaki, Z., Miranda-Barbosa, E., Shortall, R., Czako, V., Telsnig, T., Vazquez-Hernandez, C., Lacal Arántegui, R., Nijs, W., Gonzalez Aparicio, I., Trombetti, M., Mandras, G., Peteves, E., Tzimas, E., 2018. EU coal regions: Opportunities and Challenges Ahead (JRC112593 EUR 29292 EN). Publications Office of the European Union, Luxembourg. https://doi.org/10.2760/064809.

Berardino, P., Fornaro, G., Lanari, R., Sansosti, E., 2002. A New Algorithm for Surface Deformation Monitoring Based on Small Baseline Differential SAR Interferograms. IEEE Trans. Geosci. Remote Sens. 40. https://doi.org/10.1109/TGRS.2002.803792.

Burgmann, R., Rosen, P.A., Fielding, E.J., 2000. Synthetic aperture Radar interferometry to measure Earth's surface topography and its deformation. Annu. Rev. Earth Planet. Sci. 28, 169–209.

Carlà, T., Farina, P., Intrieri, E., Botsialas, K., Casagli, N., 2017. On the monitoring and early-warning of brittle slope failures in hard rock masses: Examples from an open-pit mine. Eng. Geol. 228, 71–81. https://doi.org/10.1016/j.enggeo.2017.08.007.

Carlà, T., Farina, P., Intrieri, E., Ketizmen, H., Casagli, N., 2018. Integration of ground-based radar and satellite InSAR data for the analysis of an unexpected slope failure in an open-pit mine. Eng. Geol . 235, 39–52. https://doi.org/10.1016/j.enggeo.2018.01.021.

Chen, C.W., Zebker, H.A., 2001. Two-dimensional phase unwrapping with use of statistical models for cost functions in nonlinear optimization. J. Opt. Soc. Am. A 18, 338–351.

Colombo, D., Macdonald, B., 2015. Using advanced InSAR techniques as a remote tool for mine site monitoring. Int. Symp. Rock Slope Stab. Open Pit Civ. Eng. 1–12.

Crosetto, M., Monserrat, O., Cuevas-González, M., Devanthéry, N., Crippa, B., 2016. Persistent Scatterer Interferometry: A review. ISPRS J. Photogramm. Remote Sens. 115, 78–89. https://doi.org/10.1016/j.isprsjprs.2015.10.011.

De Zan, F., Monti Guarnieri, A., 2006. TOPSAR: Terrain Observation by Progressive Scans. IEEE Trans. Geosci. Remote Sens. 44, 2352–2360. https://doi.org/10.1109/TGRS.2006.873853.

Donahue, M., 2018. Ancient Forest Home of Squatter Communities Is Doomed by Coal [WWW Document]. Natl. Geogr. Mag. URL. https://www.nationalgeographic.com/news/2018/04/hambach-forest-germany-logging-coal-conservation-science/.

Dong, J., Zhang, L., Tang, M., Liao, M., Xu, Q., Gong, J., Ao, M., 2018. Mapping landslide surface displacements with time series SAR interferometry by combining persistent and distributed scatterers: A case study of Jiaju landslide in Danba. China. Remote Sens. Environ. 205, 180–198. https://doi.org/10.1016/j.rse.2017.11.022.

Esch, C., Köhler, J., Gutjahr, K., Schuh, W.D., 2020. One-step three-dimensional phase unwrapping approach based on small baseline subset interferograms. Remote Sens. 12. https://doi.org/10.3390/RS12091473.

Esch, C., Köhler, J., Gutjahr, K., Schuh, W.D., 2019. On the analysis of the phase unwrapping process in a D-InSAR stack with special focus on the estimation of a motion model. Remote Sens. 11. https://doi.org/10.3390/rs11192295.

Ferretti, A., Prati, C., Rocca, F., 2001. Permanent Scatters in SAR Interferometry. IEEE Trans. Geosci. Remote Sens. 39, 8–20. https://doi.org/10.1109/36.898661.

Fuhrmann, T., Garthwaite, M.C., 2019. Resolving three-dimensional surface motion with InSAR: Constraints from multi-geometry data fusion. Remote Sens. 11. https://doi.org/10.3390/rs11030241.

Funning, G.J., Parsons, B., Wright, T.J., 2007. Fault slip in the 1997 Manyi, Tibet earthquake from linear elastic modelling of InSAR displacements. Geophys. J. Int. 169, 988–1008. https://doi.org/10.1111/j.1365-246X.2006.03318.x.

Haghighi, M.H., Motagh, M., 2017. Sentinel-1 InSAR over Germany: Large-scale interferometry, atmospheric effects, and ground deformation mapping. ZFV - Zeitschrift fur Geodasie, Geoinf. und Landmanagement 142, 245–256. https://doi.org/10.12902/zfv-0174-2017.

Haghshenas Haghighi, M., Motagh, M., 2019. Ground surface response to continuous compaction of aquifer system in Tehran, Iran: Results from a long-term multi-sensor InSAR analysis. Remote Sens. Environ. 221, 534–550. https://doi.org/10.1016/j.rse.2018.11.003.

Hooper, A., Segall, P., Zebker, H., 2007. Persistent scatterer interferometric synthetic aperture radar for crustal deformation analysis, with application to Volcán Alcedo, Galápagos. J. Geophys. Res. Solid Earth 112, 1–21. https://doi.org/10.1029/2006JB004763.

Hu, H., 2013. Deformation monitoring and modeling based on LiDAR data for slope stability assessment Von der Fakultät für Georessourcen und Materialtechnik der Rheinisch -Westfälischen Technischen Hochschule Aachen zur Erlangung des akademischen Grades eines Doktors de.

Intrieri, E., Carlà, T., Farina, P., Bardi, F., Ketizmen, H., Casagli, N., 2019. Satellite Interferometry as a Tool for Early Warning and Aiding Decision Making in an Open-Pit Mine. IEEE J. Sel. Top. Appl. Earth Obs. Remote Sens. 1–11. https://doi.org/10.1109/JSTARS.2019.2953339.

Jin, L., Funning, G.J., 2017. Testing the inference of creep on the northern Rodgers Creek fault, California, using ascending and descending persistent scatterer InSAR data. J. Geophys. Res. Solid Earth 122, 2373–2389. https://doi.org/10.1002/2016JB013535.

Lenk, S., Wisotzky, F., 2011. Chemical modelling of the groundwater composition in aquifers affected by lignite mine dumps discharge (surface mine Inden, Germany). Environ. Earth Sci. 62, 581–591. https://doi.org/10.1007/s12665-010-0549-8.

Liu, P., Li, Z., Hoey, T., Kincal, C., Zhang, J., Zeng, Q., Muller, J.P., 2012. Using advanced inSAR time series techniques to monitor landslide movements in Badong of the Three Gorges region. China. Int. J. Appl. Earth Obs. Geoinf. 21, 253–264. https://doi.org/10.1016/j.jag.2011.10.010.

Massonnet, D., Feigl, K.L., 1998. Radar interferometry and its application to changes in the Earth's surface. Rev. Geophys. 36, 441–500.

Massonnet, D., Rossi, M., Carmona, C., Adragna, F., Peltzer, G., Feigl, K., Rabaute, T., 1993. The displacement field of the Landers earthquake mapped by radar interferometry. Nature 364, 138–142.

Motagh, M., Bahroudi, A., Haghighi, M.H., Samsonov, S., Fielding, E., Wetzel, H.U., 2015. The 18 August 2014 Mw 6.2 Mormori, Iran, Earthquake: A thin-skinned faulting in the zagros mountain inferred from InSAR measurements. Seismol. Res. Lett. 86, 775–782. https://doi.org/10.1785/0220140222.

Motagh, M., Djamour, Y., Walter, T.R., Wetzel, H.-U., Zschau, J., Arabi, S., 2007. Land subsidence in Mashhad Valley, northeast Iran: results from InSAR, levelling and GPS. Geophys. J. Int. 168, 518–526.

Motagh, M., Shamshiri, R., Haghshenas Haghighi, M., Wetzel, H.-U., Akbari, B., Nahavandchi, H., Roessner, S., Arabi, S., 2017. Quantifying groundwater exploitation

induced subsidence in the Rafsanjan plain, southeastern Iran, using InSAR time-series and in situ measurements. Eng. Geol. 218, 134–151. https://doi.org/10.1016/J.ENGGEO.2017.01.011.

Motagh, M., Walter, T.R., Sharifi, M.A., Fielding, E., Schenk, A., Anderssohn, J., Zschau, J., 2008. Land subsidence in Iran caused by widespread water reservoir overexploitation. Geophys. Res. Lett. 35, L16403. https://doi.org/10.1029/2008GL033814.

Motagh, M., Wetzel, H.U., Roessner, S., Kaufmann, H., 2013. A TerraSAR-X InSAR study of landslides in southern Kyrgyzstan, Central Asia. Remote Sens. Lett. 4, 657–666. https://doi.org/10.1080/2150704X.2013.782111.

Mura, J., Paradella, W., Gama, F., Silva, G., Galo, M., Camargo, P., Silva, Arnaldo, Silva, Aristotelina, 2016. Monitoring of Non-Linear Ground Movement in an Open Pit Iron Mine Based on an Integration of Advanced DInSAR Techniques Using TerraSAR-X Data. Remote Sens. 8, 409. https://doi.org/10.3390/rs8050409.

NASA, 2020. Sizing up the Landslide at Bingham Canyon Mine [WWW Document]. URL. https://earthobservatory.nasa.gov/images/81364/sizing-up-the-landslide-at-bingham-canyon-mine.

Ole, T., 2011. GNU Parallel: The Command-Line Power Tool. login USENIX Mag. 36, 42–47.

Osmanoğlu, B., Sunar, F., Wdowinski, S., Cabral-Cano, E., 2016. Time series analysis of InSAR data: Methods and trends. ISPRS J. Photogramm. Remote Sens. 115, 90–102. https://doi.org/10.1016/j.isprsjprs.2015.10.003.

Paradella, W.R., Ferretti, A., Mura, J.C., Colombo, D., Gama, F.F., Tamburini, A., Santos, A.R., Novali, F., Galo, M., Camargo, P.O., Silva, A.Q., Silva, G.G., Silva, A., Gomes, L.L., 2015. Mapping surface deformation in open pit iron mines of Carajás Province (Amazon Region) using an integrated SAR analysis. Eng. Geol. 193, 61–78. https://doi.org/10.1016/j.enggeo.2015.04.015.

Peltzer, G., Rosen, P., 1995. Surface Displacement of the 17 May 1993 Eureka Valley, California, Earthquake Observed by SAR Interferometry. Science (80) 268 (5215), 1333–1336.

Przylucka, M., Herrera, G., Graniczny, M., Colombo, D., Béjar-Pizarro, M., 2015. Combination of conventional and advanced DInSAR to monitor very fast mining subsidence with TerraSAR-X data: Bytom City (Poland). Remote Sens. 7, 5300–5328. https://doi.org/10.3390/rs70505300.

Ross, Z.E., Idini, B., Jia, Z., Stephenson, O.L., Zhong, M., Wang, X., Zhan, Z., Simons, M., Fielding, E.J., Yun, S., Hauksson, E., Moore, A.W., 2019. Hierarchical interlocked orthogonal faulting in the 2019 Ridgecrest earthquake sequence. Science 351 (80), 346–351.

RWE, 2018. RWE Power AG company webpage. [WWW Document]. URL. https://www.group.rwe/en/our-portfolio/our-sites/hambach-mine-site.

Sánchez-Gámez, P., Navarro, F.J., 2017. Glacier surface velocity retrieval using D-InSAR and offset tracking techniques applied to ascending and descending passes of sentinel-1 data for southern ellesmere ice caps, Canadian Arctic. Remote Sens. 9, 1–17. https://doi.org/10.3390/rs9050442.

Sandwell, D., Mellors, R., Tong, X., Wei, M., Wessel, P., 2011. Open Radar Interferometry Software for Mapping Surface Deformation. Eos, Trans. Am. Geophys. Union 92 2011–2011.

Schaefer, L.N., Di Traglia, F., Chaussard, E., Lu, Z., Nolesini, T., Casagli, N., 2019. Monitoring volcano slope instability with Synthetic Aperture Radar: A review and new data from Pacaya (Guatemala) and Stromboli (Italy) volcanoes. Earth-Science Rev. 192, 236–257. https://doi.org/10.1016/j.earscirev.2019.03.009.

SCMP, 2018. At least 27 feared dead in landslide at Myanmar jade mine. [WWW Document]. URL. https://www.scmp.com/news/asia/southeast-asia/article/2156774/least-27-feared-dead-landslide-myanmar-jade-mine.

Tang, W., Liao, M., Yuan, P., 2016. Atmospheric correction in time-series SAR interferometry for land surface deformation mapping - A case study of Taiyuan. China. Adv. Sp. Res. 58, 310–325. https://doi.org/10.1016/j.asr.2016.05.003.

Tong, X., Schmidt, D., 2016. Active movement of the Cascade landslide complex in Washington from a coherence-based InSAR time series method. Remote Sens. Environ. 186, 405–415. https://doi.org/10.1016/j.rse.2016.09.008.

Tymofyeyeva, E., Fialko, Y., 2015. Mitigation of atmospheric phase delays in InSAR data, with application to the eastern California shear zone. J. Geophys. Res. Solid Earth 120, 5952–5963. https://doi.org/10.1002/2015JB011886.

Walter, T.R., Haghshenas Haghighi, M., Schneider, F.M., Coppola, D., Motagh, M., Saul, J., Babeyko, A., Dahm, T., Troll, V.R., Tilmann, F., Heimann, S., Valade, S., Triyono, R., Khomarudin, R., Kartadinata, N., Laiolo, M., Massimetti, F., Gaebler, P., 2019. Complex hazard cascade culminating in the Anak Krakatau sector collapse. Nat. Commun. 10. https://doi.org/10.1038/s41467-019-12284-5.

Wang, T., Shi, Q., Nikkhoo, M., Wei, S., Barbot, S., Dreger, D., Bürgmann, R., Motagh, M., Chen, Q.F., 2018. The rise, collapse, and compaction of Mt. Mantap from the 3 September 2017 North Korean nuclear test. Science 361 (80), 166–170. https://doi.org/10.1126/science.aar7230.

Wasowski, J., Bovenga, F., 2014. Investigating landslides and unstable slopes with satellite Multi Temporal Interferometry: Current issues and future perspectives. Eng. Geol. 174, 103–138. https://doi.org/10.1016/j.enggeo.2014.03.003.

Wessel, B., Huber, M., Wohlfart, C., Marschalk, U., Kosmann, D., Roth, A., 2018. Accuracy assessment of the global TanDEM-X Digital Elevation Model with GPS data. ISPRS J. Photogramm. Remote Sens. 139, 171–182. https://doi.org/10.1016/j.isprsjprs.2018.02.017.

Wessel, P., Luis, J., Uieda, L., Scharroo, R., Wobbe, F., Smith, W.H.F., Tian, D., 2019. The Generic Mapping Tools Version 6. Geochemistry, Geophys. Geosystems. https://doi.org/10.1029/2019GC008515.

Vinzelberg, G., Dahmen, D., 2014. The Inden Residual Lake and the Federal Autobahn A44n – Geotechnical Requirements to Be Met by Large-Scale Structures in the Rhenish Lignite Mining Area. In: Proceedings of the 12th International Symposium Continuous Surface Mining. Springer, Aachen, Germany. pp. 91–100. https://doi.org/10.1007/978-3-319-12301-1_10.

Xu, X., Sandwell, D.T., Tymofyeyeva, E., Gonzalez-Ortega, A., Tong, X., 2017. Tectonic and Anthropogenic Deformation at the Cerro Prieto Geothermal Step-Over Revealed by Sentinel-1A InSAR. IEEE Trans. Geosci. Remote Sens. 55, 5284–5292. https://doi.org/10.1109/tgrs.2017.2704593.

Yague-Martinez, N., Prats-Iraola, P., Gonzalez, F.R., Brcic, R., Shau, R., Geudtner, D., Eineder, M., Bamler, R., 2016. Interferometric Processing of Sentinel-1 TOPS Data. IEEE Trans. Geosci. Remote Sens. 54, 2220–2234. https://doi.org/10.1109/TGRS.2015.2497902.

Yang, Z., Li, Z., Zhu, J., Yi, H., Hu, J., Feng, G., 2017a. Deriving dynamic subsidence of coal mining areas using InSAR and logistic model. Remote Sens. 9. https://doi.org/10.3390/rs90201025.

Zhang, Z., Wang, C., Tang, Y., Fu, Q., Zhang, H., 2015b. Subsidence monitoring in coal area using time-series InSAR combining persistent scatterers and distributed scatterers. Int. J. Appl. Earth Obs. Geoinf. 39, 49–55. https://doi.org/10.1016/j.jag.2015.02.007.

Yang, Z., Li, Z., Zhu, J., Yi, H., Hu, J., Feng, G., 2017b. Deriving dynamic subsidence of coal mining areas using InSAR and logistic model. Remote Sens. 9. https://doi.org/10.3390/rs90201025.

Zhang, Z., Wang, C., Tang, Y., Fu, Q., Zhang, H., 2015a. Subsidence monitoring in coal area using time-series InSAR combining persistent scatterers and distributed scatterers. Int. J. Appl. Earth Obs. Geoinf. 39, 49–55. https://doi.org/10.1016/j.jag.2015.02.007.

Zhu, C., Wang, Z., Li, P., Motagh, M., Zhang, L., Jiang, Z., Long, S., 2020. Retrieval and Prediction of Three-Dimensional Displacements by Combining the DInSAR and Probability Integral Method in a Mining Area. IEEE J. Sel. Top. Appl. Earth Obs. Remote Sens. 13, 1206–1217. https://doi.org/10.1109/JSTARS.2020.2978288.